EXPERIMENTAL STUDY OF NANOSCALE METAL CLUSTERS USING SYNCHROTRON RADIATION EXCITED PHOTOELECTRON SPECTROSCOPY

MIKKO-HEIKKI MIKKELÄ

Department of Physics
University of Oulu
Finland

Academic Dissertation to be presented with the assent of the Faculty of Science, University of Oulu, for public discussion in the Auditorium L10, on February 1st, 2013, at 12 o'clock noon.

REPORT SERIES IN PHYSICAL SCIENCES Report No. 81
OULU 2013 • UNIVERSITY OF OULU

Opponent
Dr. Matthias Neeb, Helmholtz-Zentrum-Berlin fuer Materialien und Energie, Germany

Reviewers
Prof. Arnaldo N. de Brito, State University of Campinas, Brazil
Dr. Robert Richter, Elettra - Sincrotrone Trieste, Italy

Custos
Prof. Marko Huttula, University of Oulu, Finland

ISBN 978-952-62-0078-1
ISBN 978-952-62-0079-8 (PDF)
ISSN 1239-4327
OULU UNIVERSITY PRESS
Oulu 2013

Mikkelä, Mikko-Heikki Johannes: Experimental study of nanoscale metal clusters using synchrotron radiation excited photoelectron spectroscopy

Department of Physics
P.O. Box 3000
FIN-90014 University of Oulu
FINLAND

Abstract

In this work an experimental study of size varied, neutral, and free metal clusters using synchrotron radiation excited photoelectron spectroscopy was performed. The combined core-level and valence photoelectron spectroscopic investigation indicates metallic properties for nanoscale Rb, K, Sn, and Bi clusters. In the case of Sn the experimental results suggest a metal-to-insulator transition occurring at the studied size range. In addition to the experimental results the technical implementation of the cluster production set-up is presented and jellium-model-based simulations are compared with the experimental results of the Rb and K clusters.

Key words: Metal clusters, cluster formation, metallic properties, synchrotron radiation, electron spectroscopy, core-level photoelectron spectroscopy, valence photoelectron spectroscopy, jellium model simulations

Acknowledgments

The present work was carried out at the Department of Physics of the University of Oulu. I would like to thank the staff of the department and Head of the Department, Prof. Matti Weckström, for placing the facilities at my disposal.

I especially want to thank my supervisor Prof. Marko Huttula for guiding me through the challenging times of the doctoral studies and research, and having all the patience and understanding which was required while working with me. I know that such a dedication to supervision and support is rare. I would like to express also my deepest gratitude to Dr. Maxim Tchaplyguine, for giving me an insight to the challenging field of cluster research and offering guidance and supervision almost in the every part of this work. Without this support many of the challenges would have been far more insurmountable than they already were. I also thank Doc. Kari Jänkälä and Doc. Samuli Urpelainen for their major contribution, help and visionary ideas which took this research to the next level.

This work is a result of an intensive teamwork and I would like to thank my colleagues Prof. Olle Björneholm, for valuable discussions and assistance, and Tomas Andersson and Chaofan Zhang for supporting the experimental work during the long days and nights at the laboratory. I also thank Dr. Sergey Osmekhin for contribution and assistance, and Dr. Leena Partanen and Lauri Hautala for the help and valuable discussions. I also appreciate the help and effort of Prof. Arnaldo N. de Brito and Dr. Robert Richter and I thank them for the critical comments and ideas which improved this work.

I would like to thank Prof. Helena Aksela and Prof. emer. Seppo Aksela for introducing me to the exciting world of electron spectroscopy and experimental physics, and for all the help during the past few years. I am also grateful for Doc. Sami Heinäsmäki and Doc. Saana-Maija Huttula for additional help and interesting discussions. As this work was based on the experimental activities, none of it would have been possible without the skills and effort of Pentti Kovala, who contributed greatly in designing and building the experimental set-ups of this work. I also admire his magical ability to devise outstanding designs from our silly and ambiguous yet ambitious ideas.

I also appreciate the mental support which I got from the other members

of the electron spectroscopy group in Oulu, and I am especially grateful for Ari Mäkinen and Antti Kettunen for the countless discussions related to my research. I have to admit that probably the most of these discussion were not work related but anyway intriguing and piquant at the intellectual level.

This work was financially supported by Vilho, Yrjö, and Kalle Väisälä Foundation, National Graduate School in Materials Physics and Research Council for Natural Sciences of the Academy of Finland, and I thank them for their support. I also thank the board and staff of the MAX IV laboratory for allowing me to carry out research at their facility and providing a dedicated and vital support.

Even though the path through the doctoral studies has been a long and challenging one, it is still only a small fraction of the bigger journey of the life during which I have received support and appreciation from my parents and the closest friends. I would like to thank my parents Markku and Hilkka for always giving me their full support and understanding, and for never trying to push me into any specific direction and thus letting me to seek freely my own aspirations. I also thank my friends Artem and Sami for understanding my lack of free time. I am also very grateful for my beloved Anna who has supported and existed for me all these long years and reminded me about the correct priorities of the life.

Oulu, Dec 2012 Mikko-Heikki Mikkelä

LIST OF ORIGINAL PAPERS

The present thesis incorporates an introductory part and the following papers, referred in the text by their Roman numerals:

I. M. Huttula, M.-H. Mikkelä, M. Tchaplyguine, and O. Björneholm: *Size-varied photoelectron spectroscopy of metal clusters using the Exchange Metal Cluster Source*, J. Electron Spectrosc. Relat. Phenom. **181**, 145 (2010).

II. M.-H. Mikkelä, M. Tchaplyguine, K. Jänkälä, T. Andersson, C. Zhang, O. Björneholm, and M. Huttula: *Size-dependent study of Rb and K clusters using core and valence level photoelectron spectroscopy*, Eur. Phys. J. D **64**, 347 (2011).

III. S. Osmekhin, M. Tchaplyguine, M.-H. Mikkelä, M. Huttula, T. Andersson, O. Björneholm, and S. Aksela: *Size-dependent transformation of energy structure in free tin clusters studied by photoelectron spectroscopy*, Phys. Rev. A **81**, 023203 (2010).

IV. M.-H. Mikkelä, M. Tchaplyguine, S. Urpelainen, K. Jänkälä, O. Björneholm, and M. Huttula: *Photoelectron spectroscopy of unsupported bismuth clusters: Size related effects of metallic properties*, J. Appl. Phys. **112**, 084326 (2012).

V. K. Jänkälä, M.-H. Mikkelä, and M. Huttula: *Valence photoionization of free, neutral, and size-varied alkali metal clusters*, J. Phys. B: At. Mol. Opt. Phys. **44**, 105101 (2011).

VI. K. Jänkälä, M. Tchaplyguine, M.-H. Mikkelä, O. Björneholm, and M. Huttula: *Photon energy dependent valence band response of metallic nanoparticles*, Phys. Rev. Lett **107**, 183401 (2011).

All the papers included in this thesis are results of teamwork. In Papers I-V the author participated in the measurements and took part in developing the experimental set-ups. In Paper I the author gave a strong contribution to the writing and performed the data analysis. The author performed the data-analysis and was the primary writer in Papers II and IV. In Papers III and V the author assisted with the data analysis and commented on the manuscript. In Paper VI the author participated in the manuscript processing and experimental preparations.

In addition to the papers mentioned above, the author has contributed to the following papers and manuscripts which are not included in this thesis:

A S. Urpelainen, S. Heinäsmäki, M.–H. Mikkelä, M. Huttula, S. Osmekhin, H. Aksela, and S. Aksela: 5*d photoionization and Auger decay in atomic Pb*, Phys. Rev. A **80**, 012502 (2009).

B C. Zhang, T. Andersson, S. Svensson, O. Björneholm, M. Huttula, M.-H. Mikkelä, M. Tchaplyguine, and G. Öhrwall: *Ionic bonding in free nanoscale NaCl clusters as seen by photoelectron spectroscopy*, J. Chem. Phys. **134**, 124507 (2011).

C M. Tchaplyguine, G. Öhrwall, T. Andersson, S. Svensson, O. Björneholm, M. Huttula, M. Mikkelä, S. Urpelainen, S. Osmekhin, A. Caló, S. Aksela, and H. Aksela: *Valence-band narrowing and metallic-screening disappearance in small Pb clusters - as seen by photoelectron spectroscopy*, Submitted for publication in Phys. Rev. B.

D C. Zhang, T. Andersson, S. Svensson, O. Björneholm, M. Huttula, M.-H. Mikkelä, D. Anin, M. Tchaplyguine, G. Öhrwall: *Holding on to Electrons in Alkali-Halide Clusters: Decreasing Polarizability with Increasing Coordination*, Accepted for publication in J. Phys. Chem. A. (2012).

E S. Urpelainen, M. Tchaplyguine, M.-H. Mikkelä, K. Kooser, T. Andersson, C. Zhang, E. Kukk, O. Björneholm, and M. Huttula: *Size evolution of electronic properties in free antimony nanoclusters*, Accepted for publication in Phys. Rev. B (2012).

F L. Partanen, M.-H. Mikkelä, M. Huttula, M. Tchaplyguine, C. Zhang, T. Andersson, and O. Björneholm: *Solvation at nanoscale: Alkali-halides in water clusters*, Accepted for publication in J. Chem. Phys. (2012).

Contents

Chapter 1

Introduction

Clusters consist of a finite and arbitrary number of constituent atoms or molecules and form an intermediate state of matter between individual atoms and the solid state. Especially for clusters made of metallic elements the cluster size is a critical property and while large clusters may have a metallic character close to that of the respective solid, smaller clusters may resemble non-metallic semiconductive particles. This phenomenon has been related to the evolution of clusters' discrete energy levels to the solid-like bands at large cluster sizes [1], and it is one of the key topics of metal cluster research.

In photoelectron spectroscopy the electronic structure of matter is probed by irradiating the investigated system by ionizing radiation and detecting the emitted photoelectrons. This technique was introduced for the chemical analysis by Siegbahn in the 1960's [2, 3] and since then it has become an established technique in the research of metal clusters [4]. Even though the first experiments on free cluster jets were already carried out by Becker in the 1950's [5], the core-level photoelectron spectroscopy of free clusters could not be performed until much later [6]. This was due to the 3rd generation synchrotron radiation sources and enhanced instrumentation offering higher signal intensities which made electron spectroscopy of these relatively dilute targets feasible. Study of free clusters located in vacuum is of great importance for the photoelectron spectroscopy, since the perturbing chemical environment (e.g. substrate) is not present - as in the case of deposited clusters on surfaces - and therefore the observed photoelectron spectra of free clusters are undisturbed and describe the properties of the studied clusters in general.

Core-level and valence photoelectron spectroscopy provides information about the clusters' electronic structure and gives an insight to the bonding mechanisms of the constituent atoms. Properties of the photoelectron spectra can be also used to probe the metallic properties of the studied clusters and obtain information about their physical dimensions [4]. Furthermore, in the case of size selected and charged clusters, the band gap closure at the valence

has been observed directly using photoelectron spectroscopy [7].

In the present work we have used the synchrotron radiation excited photoelectron spectroscopy to probe the metallic properties of free and neutral Rb, K, Sn and Bi metal clusters in nanoscale dimensions. The high brightness and energy tunability of the synchrotron radiation has made it possible to study both the deep core-level and the outer valence orbitals and has provided a unified picture of the evolution of clusters' properties as a function of cluster size. Moreover, jellium-model-based simulations have been carried out and compared with the experimental results. In addition to the scientific discoveries a great part of this work was to develop, build and test the used cluster source set-up which is capable to produce free and size varied clusters from various elements and to provide adequate sample densities for the core-level and valence photoelectron spectroscopy.

The introductory part of the thesis is arranged into six chapters. In Chapter 2, *Methods and concepts*, the main principles concerning the photoelectron spectroscopy of free metal clusters are treated. In Chapters 3, *Cluster formation*, and 4, *Experiments and instrumentation*, the cluster formation techniques and the experimental set-ups and instrumentation used in Papers I-VI are presented and discussed. And finally, in Chapters 5, *Summary and discussion of the included papers*, and 6, *Conclusion and outlook*, the results of the Papers I-VI and the outlook of future plans are briefly discussed.

Chapter 2

Methods and concepts

2.1 Electronic structure of matter

2.1.1 Schrödinger equation and electronic orbitals

In the theory of quantum mechanics all physical systems, such as atoms, molecules and clusters, can be characterised by a wave function Ψ. In non-relativistic case the wave function can be obtained by solving the time-independent Schrödinger equation [8, 9]:

$$\hat{H}\Psi = E\Psi, \tag{2.1}$$

where $\hat{H}$ is Hamiltonian operator of the system, and eigenvalue E is the total energy of the system. Hamiltonian operator depends on the investigated system and includes all the interactions.

The Schrödinger equation can be solved in a closed-form only in the case of a single electron systems (e.g. hydrogen) and typically solutions for more complex systems which include electron-electron interaction - such as multi-electron atoms, molecules and clusters - require various approximations and initial guesses for the wave functions. In the Hartree-Fock method the electron-electron interaction is replaced by a central field approximation and Schrödinger equation is typically solved using variational principle and iterative approach. For heavy systems where relativistic approach is required, the Dirac-Fock theory [10] can be used and the Schrödinger equation is replaced by the Dirac equation.

Electronic configurations and coupling schemes in atoms

Atomic electrons' wave functions, orbitals, can be described in terms of the so-called *quantum numbers* which correspond to the conserved quantities of the system in dynamical processes. In the case of atoms the following quantum numbers are defined [9]: The principle quantum number $n = 1, 2, 3, ...,$

the angular momentum quantum number $0 \leq l \leq n-1$, the magnetic quantum number $-l \leq m_l \leq l$, which is a projection of the angular momentum, and the spin quantum number $m_s = \pm 1/2$ which relates to the projection of electrons' inherent angular momentum. Additionally the angular quantum numbers are typically designated by alphabetical letters as $s, p, d, f...$ for $l = 0, l = 1, l = 2, l = 3, ...$, respectively [9].

The orbitals are occupied by electrons via Aufbau ("building up") and Pauli's exclusion principles and this forms a system with a specific *electronic configuration* which can be described in terms of the orbitals' quantum numbers. In the case of atoms the configurations are nominated by nl_j^k notation, where k is the total number of electrons per orbital defined by the principle quantum number n and $j = l + m_s$. For example, by using this notation we get for atomic Rb the electron configuration: $1s^2_{1/2}2s^2_{1/2}2p^2_{1/2}2p^4_{3/2}3s^2_{1/2}3p^2_{1/2}$ $3p^4_{3/2}3d^4_{3/2}3d^6_{5/2}4s^2_{1/2}4p^2_{1/2}4p^4_{3/2}5s^1_{1/2}$. Here, the outermost shell ($5s$) is called as a *valence orbital* and the inner shells ($1s - 4p$) as *core-level orbitals*, and the electrons occupying these states are called valence and core-level electrons, respectively. The orbitals energetically close to the valence are sometimes also called as *inner valence* orbitals.

In order to describe the specific states belonging to a single electronic configuration, angular momenta are usually coupled in the so-called LS- or jj-coupling schemes. In the LS-coupling the orbital angular momentum $\mathbf{l}$ and spin angular momentum $\mathbf{s}$ are coupled separately and give the total angular momentum $\mathbf{J} = \mathbf{L} + \mathbf{S}$, where $\mathbf{L} = \sum \mathbf{l_i}$ and $\mathbf{S} = \sum \mathbf{s_i}$. In the jj-coupling the $\mathbf{l}$ and $\mathbf{s}$ are coupled individually to $\mathbf{j_i} = \mathbf{l_i} + \mathbf{s_i}$ and the total momentum is then $\mathbf{J} = \sum \mathbf{j_i}$. LS-coupling is more appropriate for light elements ($Z < 30$) where Coulomb interaction is strong in comparison to spin-orbit interaction and jj-coupling is better for heavier elements with a strong spin-orbit interaction.[9]

Molecular orbitals

In the case of multi-atom systems further approximations, such as the Born-Oppenheimer approximation [11] which separates the nuclear and electronic wave functions, are usually applied. Moreover, instead of atomic-like orbitals molecules are described by *molecular orbitals* and the molecular orbitals can be described, for example, as a linear combinations of atomic orbitals (LCAO)[11].

For molecules and small clusters the energy levels of the molecular orbitals are very discrete and approach more band-like structure when the number of the constituents is increased. This effect is discussed later in Section 2.2.4 where we treat the energy difference between the highest occupied molecular orbitals (HOMO) and the lowest unoccupied molecular orbitals (LUMO) as a function of cluster size.

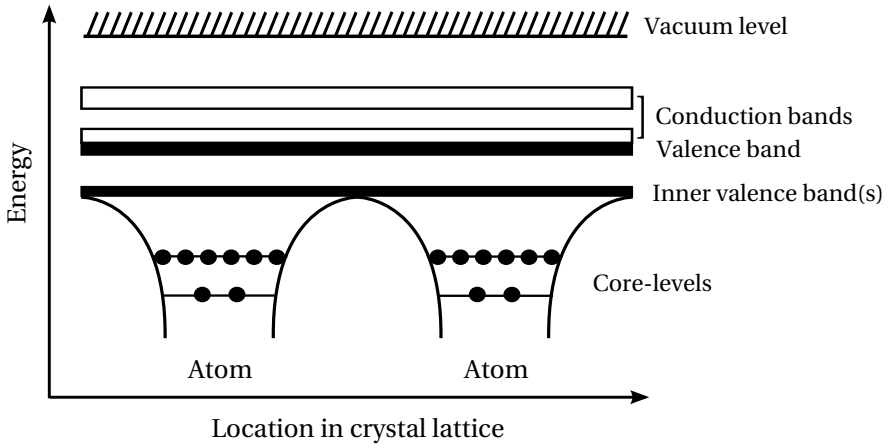

Figure 2.1: Schematic illustration of discrete and band energy levels in solid state.

2.1.2 Relevant aspects of band theory and metallicity in solid state

In solid state the core-level electrons are located on localized atomic- or molecular-like discrete orbitals. However the uppermost valence or inner-valence electrons may occupy states which are so densely packed that they form continuous energy intervals, so-called *bands* [12, 13]. In principle an infinite number of bands exists but typically only few bands are completely or partially occupied by electrons and the uppermost band is called *valence band*. The rest of the bands are vacant and they are called *conduction bands*. A schematic illustration of core-level and valence energy levels in metal-like solid is shown in Figure 2.1. Since the occupation of the solid state valence bands cannot be described by discrete integer numbers therefore the *density of states* (DOS) is typically used which describes the number of states per a unit of energy.

Metallicity

Using a simple band model the solid state matter can be classified according to their valence and conduction band structure and the magnitude of the band gap of the latter two bands into following four categories : *metals*, *semimetals*, *semi-conductors* and *insulators* [12]. Different kinds of solid state classifications are illustrated in Figure 2.2.

In metals the occupied valence band is either partially filled or, in other words, the valence band and the empty conduction band overlap. By definition metals have high electric conductivity at absolute zero temperature when infinitely low static electric field is applied. High conductivity is due

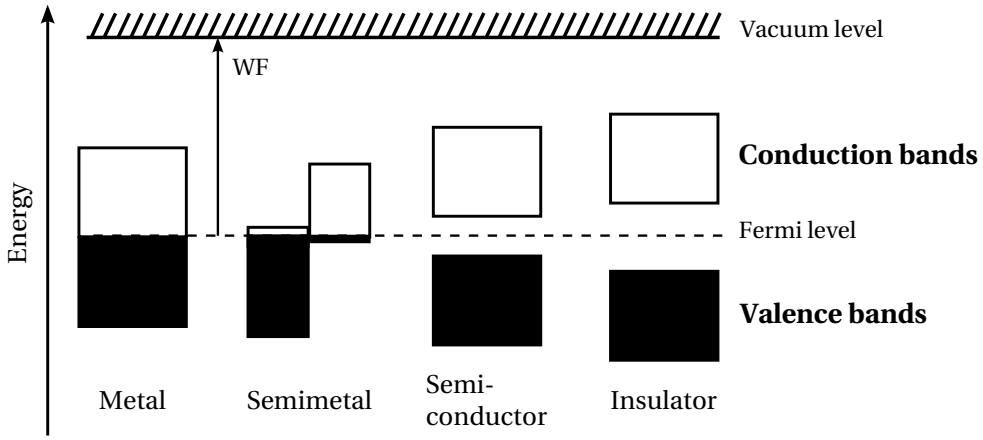

Figure 2.2: Schematic presentation of the valence and conduction bands in the different types of solid states at 0 K temperature.

to the fact that the valence electrons are highly mobile and act as a free electron gas in positive-ion-core lattice [12]. Like metals, also semimetals are metal-like and possess non-zero conductivity. However the valence and the conduction bands have a so-called indirect overlap in the momentum space of conduction electrons and this causes part of the valence band electrons to reside at the bottom of the conduction band inducing electron hole states at the top of the valence band. In semimetals both positive electron holes and negative electrons act as a charge carriers but typical electric conductivities are smaller for semimetals than metals [12].

For semi-conductors the valence and the conduction bands are separated in energy by a band gap which restricts the mobility of valence electrons to empty conduction states and therefore semiconductors are not conductive at absolute zero temperature [12]. However band gaps of semiconductors are relatively small and at higher temperatures the valence electrons may be excited thermally to the conduction band states and therefore at non-zero temperatures semi-conductors can be conductive. The band structure of insulators and semi-conductors is otherwise very similar except the band gap of insulators is larger and therefore insulators are non-conductive even at high temperatures [12].

Work function

Work function designates the energy which is required to remove an electron from the Fermi level of a sample under investigation, such as a solid or a cluster, to the vacuum zero level [12]. In Figure 2.2 the work function and the location of Fermi level in different kinds of solids are illustrated.

2.2 Metal clusters

2.2.1 Bonding in clusters

Molecules, clusters and solid state objects are all assembled from individual atoms which are bound together by various kinds of bonding mechanisms. The interatomic forces are defined mostly by the atoms' uppermost valence electrons and are usually very characteristic for each element. [12, 13]

Conventionally the bonding forces are divided into four main categories according to their bonding mechanisms and the strength of the bonding: *covalent*, *ionic*, *metallic* and *van der Waals* bonding [12, 13]. This is done even though in principle the bonding mechanisms cannot be separated so rigorously and usually the elements may pose several bonding characters at the same time. However, in practice this kind of classification provides a viable tool to describe the typical chemical and physical properties of different elements.

The *van der Waals* bonding is typical for rare gas atoms and it is the weakest of the four main bonding mechanisms. Attractive van der Waals force is induced between the bound atoms due to dipole-dipole interaction which is caused by the polarization of the atoms' electron clouds [12, 13].

In the metallic and covalent bonding the charges of the valence electrons are shared between the constituent atoms in the cluster and in principle the covalent and metallic bonding are very similar and differ in the extent of the charge sharing. In the metallic bonding the valence electrons are not bound to any specific atom-core but are instead delocalized across the whole solid or large cluster and shared between all positively charged ion-cores [12, 13]. The most ideal metallically bound substances are monovalent alkali-metals while for the other metal-elements delocalization of the valence electrons is not as simple. In the case of covalent bonding the valence electrons are mostly shared between the nearest atoms and are relatively localized. Especially semi-conductor elements, such as Si, are bound in the solid covalently [12, 13]. In the case of very small clusters, consisting of metal atoms, separating covalent and metallic bonding between the constituent atoms can be challenging, because typically at this size regime clusters of metallic- and semi-conductor elements can pose similar bonding mechanisms. [13]

The main principle of ionic bonding is the charge *transfer* between the atoms involved. The ionic bonding can occur between two different kinds of atoms where the valence electron of one of the atoms is so loosely bound that it is energetically favourable for it to be bound to another atom (participating in the bond) with deeper valence states. In this case a charge transfer takes place and the atoms are bound by electrostatic attraction between oppositely charged species. Alkali-halides which consist of bound alkali-metal and halogen group atoms are the most typical elements for the ionic bond-

Type	Strength	Example
Ionic	$2-4$ eV	NaCl, KCl, NaI ...
Covalent	$1-4$ eV	C_{60}, S
Metallic	$0.5-3$ eV	Na, Al, Ag, Cu, Pt
van der Waals	≤ 0.3 eV	He, Ne, Ar, Xe, Kr

Table 2.1: Typical bonding strengths and examples of the main four bonding mechanisms [13].

ing. Different bonding categories, their characteristic strengths and some examples of typical elements are presented in the Table 2.1.

2.2.2 Geometric structure

The most common lattice symmetries for solid metals are *face-centered cubic* (fcc) (e.g. group 10 & 11 transition metals), *body-centered cubic* (bcc) (e.g. alkali-metals) and *hexagonal close packing* (hcp) (e.g. Be, Mg, Zn, Cd) [12]. In addition to these symmetries some metals follow more unusual structures, such as *tetragonal* (e.g. β-Sn) [14] and *rhombohedral* (e.g. Bi) [12].

Lattice structures of nanoscale clusters can deviate from the corresponding solid symmetries and typically pose symmetries which are not found in solids, such as icosahedral symmetry [15–18]. Especially small clusters can have various kinds of symmetries and the symmetry may be very size dependent. For larger clusters the interatomic distances and lattice symmetry is expected to approach solid properties at some size regime, characteristic for each element [19–22]. Depending on the experimental conditions metal clusters can be also in a melted state and therefore lacking any kind of lattice structure [23].

2.2.3 Jellium electronic shell model and magic numbers of metal clusters

The electronic structure of "simple-metal" metal clusters, such as alkali metal clusters, can be explained using the so-called jellium model, where the cluster electrons are held together in a uniform spherical square well potential created by the positive ion-cores and independent delocalized valence electrons [24, 25]. In this model the valence electrons occupy specific orbitals or shells which can be characterized by a radial quantum number and an angular momentum (1s, 1p, 1d, 2s, 1f, 2p, 1g, 2d, 1h, ...). For each angular momentum l there are $(2l+1)$ degenerate orbitals, which together constitute a shell. With increasing cluster size more and more of the orbitals are occupied [26]. This behaviour was for the first time experimentally confirmed by Knight et al. in 1984 for Na clusters [27] for which specific abundancies were observed in

the mass spectra due to the closing of the electron shells. Cluster sizes corresponding to these closed electronic shells are called *magic numbers* and are found to be physically and chemically stable [28]. Such electronic structure of clusters has been confirmed also by the observations of ionization energies and electron affinities as a function of cluster size. Typically the term "magic numbers" is also used for clusters which have closed geometric shell structure, as in the case of icosahedral symmetry.

In Papers V and VI the jellium-model-based calculations are found to describe well the experimental response of nanoscale Rb and K clusters. The results and the applied calculations are discussed more in detail in Section 5.2.2.

2.2.4 Metal-to-insulator transition

At sufficiently small sizes metal clusters can become non-metallic, moreover metallicity of clusters can oscillate as a function of cluster size: it can become periodically either metallic or non-metallic with the decreasing size [1, 29]. At larger cluster sizes the HOMO-LUMO gap changes typically in a more monotonic way [1]. This transition from metallic to insulating properties is known as metal-to-insulator transition (MIT) and it is one of the key topics of this work. Multiple reasons why MIT occurs in nanoscale entities have been addressed and they are related to a change of coordination numbers and energy level structure such as, for example hybridization of the uppermost orbitals close to the Fermi level, as observed for bivalent Zn, Mg and Hg clusters [1].

Clusters of monovalent metals such as alkali and noble metals, have been found to pose oscillating metallic behaviour at small cluster sizes and most of the clusters with the sizes equal to magic numbers have been found to be non-metallic [1]. Metallic properties for Rb and K clusters, close to this size regime, are supported by Paper II of this work. In Paper III the MIT of Sn clusters approximately at cluster size of $N = 40$, has been observed this result being consistent with the previous work on anionic Sn clusters [30]. Furthermore in Paper IV metallic properties of Bi clusters have been disclosed down to size of few tens of atoms per cluster so no sign of MIT in the studied size range and conditions are observed.

2.3 Photoelectron spectroscopy of metal clusters

Photoelectron spectroscopy is a viable tool for investigating electronic structure of a wide range of objects, such as atoms, molecules, clusters and solids [2, 3]. The most distinct influence on photoelectron spectra of metal clus-

ters has the local chemical environment, and various final state effects of the photoionization [4, 31]. Furthermore, dynamics of the valence electrons and cluster size distribution can have pronounced effects on the observations. Information obtained from the core-level and valence is complementary and therefore in order to carry out a comprehensive study of metallic properties of metal clusters both types of levels should be investigated concurrently. This has been approached in Papers I-VI in which various properties of core-level and valence spectra of metal clusters have been investigated.

2.3.1 Photoionization and excitation

The photoelectron spectroscopy is based on the *photoelectric effect*, which was observed experimentally for the first time by H. Hertz in 1887 [32] and was later theoretically explained by A. Einstein in 1905 [33]. In a photoionization process a target such as atom, molecule, cluster or solid, is irradiated by energetic photons - typically from ultraviolet to hard X-ray radiation - which may lead to a removal of a bound electron from the system. In such a process a photon of the exciting radiation is absorbed and the energy of the photon is transferred to the electronic system. If the energy of the incoming photon is higher than the binding energy of the electron ($h\nu > E_b$) the electron is ejected out of the system and the system is left in an *ionized* state and often also in an *excited* state [9]:

$$A + h\nu \rightarrow A^{+*} + e^{-}. \tag{2.2}$$

Moreover, the excess energy of the photon is transformed into the kinetic energy of the outgoing electron [9]:

$$E_{kin} = h\nu - E_{bin} = h\nu - (E_f - E_i). \tag{2.3}$$

Here E_{bin} is defined as the binding energy of the electron and E_i and E_f are the total energies of the initial and final state of the system, respectively. Schematic illustrations of core-level and valence photoionizations in an atom are shown in Figure 2.3 a-b).

Apart from a direct photoionization, incoming photons may also excite the system by promoting a bound electron from a lower core-level or valence energy state into a higher energy state in a process which is called *photoexcitation* [9]:

$$A + h\nu \rightarrow A^{*}. \tag{2.4}$$

This kind of process leaves the system in an excited state which will decay ultimately into a non-excited state via different decay mechanisms. Photoexcitation of a core-level electron to an higher vacant, so-called *Rydberg state*, is illustrated in Figure 2.3.

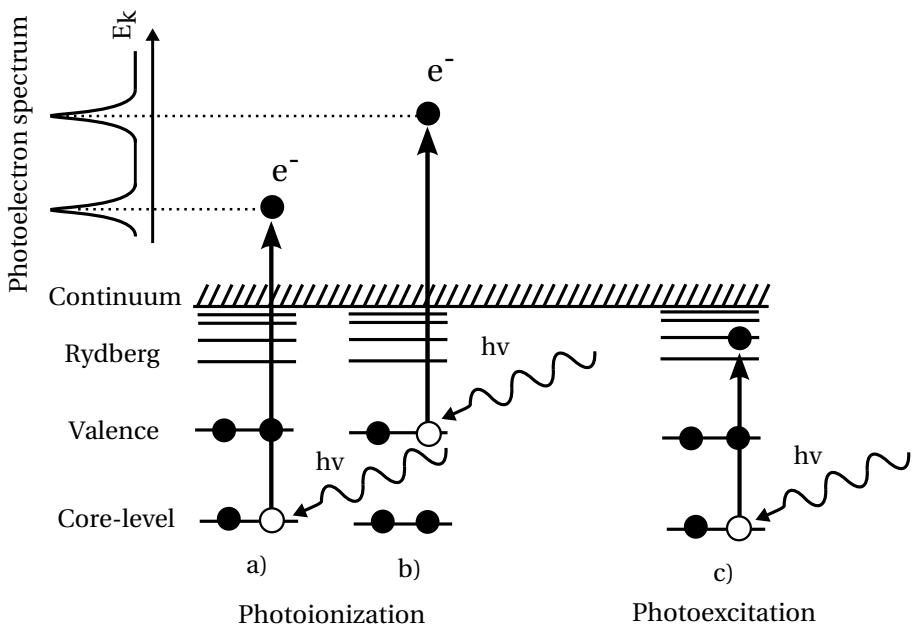

Figure 2.3: Schematic view of a core-level a) and valence b) photoionization, and photoexcitation c) in an atom.

Transition probabilities and angular distribution

In quantum mechanics the probability of a transition between an initial and a final state of a system, caused by a time-independent operator $\hat{V}$, is determined by the so-called *Fermi's golden rule* [9]:

$$P_{i\to f} \propto |\langle \Psi_f | \hat{V} | \Psi_i \rangle|^2, \tag{2.5}$$

where Ψ_i and Ψ_f are the initial and final state wave functions of the system, respectively. This relation determines also the transition probabilities of photoionization and photoexcitation processes and typically the transition probabilities are described by *cross sections*. [9]

If the wavelength of the exciting radiation is much larger than the dimensions of the atom, then the so-called *dipole approximation* [9] is valid which yields specific selection rules between the initial and final states. In the dipole approximation with linearly polarized radiation the angular distribution (i.e. differential cross sections at angle θ) of the electron emission can be described by the following formula [9]:

$$\frac{d\sigma}{d\Omega} = \frac{\sigma(h\nu)}{4\pi}\left[1 + \beta P_2(\cos\theta)\right] \tag{2.6}$$

where β is the so-called angular anisotropy parameter describing the angular distribution of the electron emission, θ is the angle between the observation

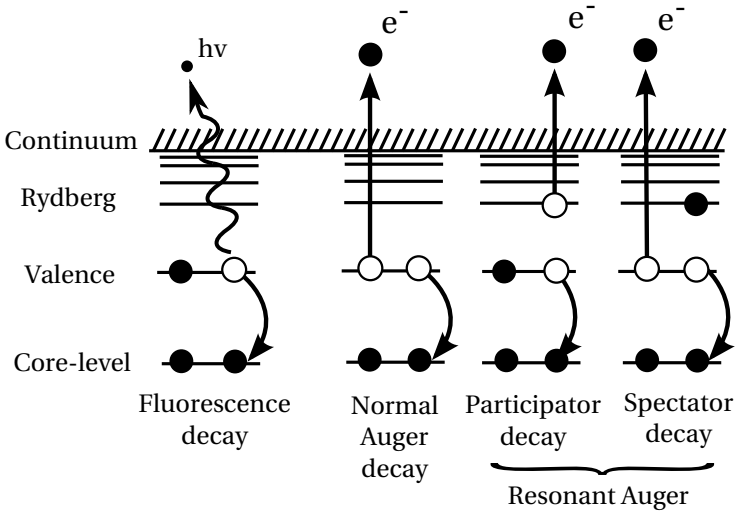

Figure 2.4: Schematic view of fluorescence decay transition and normal and two different resonant Auger decays transitions following the initial core-level photoionized state.

and the electric field vector of the exciting radiation, P_2 is the second order Legendre polynomial and $\sigma(h\nu)$ is the photon energy dependent total cross section. With the so-called *magic angle* value $\theta \approx 54.7°$ the term $P_2(\cos\theta) = 0$ and the angular dependence of the differential cross sections disappears.

2.3.2 Fluorescence and Auger decay

After photoionization or excitation the electronic system is typically left in an excited state which is unstable and will decay into an energetically lower excited or non-excited state. Decay of an excited state can occur either by radiative *fluorescence decay* involving emission of a photon or by *Auger decay* involving emission of an electron [9]. Schematic presentation of the decay mechanisms are illustrated in Figure 2.4.

In the final state of a photoionization or photoexcitation a vacancy exists at core-level or valence states of the system. If the vacancy is in a core-level orbital it is filled by an electron lying at energetically higher state. This is the first stage of the so-called Auger and fluorescence decays [9].

Auger decay transitions are divided into two categories, so-called *normal Auger transitions* and *resonant Auger transitions*. In a normal Auger transition the core-level vacancy of a photoionized state is filled up by a core-level or valence electron and as a subsequent result another electron is ejected out of the system. This emitted electron is called *Auger electron* and its kinetic energy is determined by the energy difference of the initial and final state of the Auger transition [9].

In the resonant Auger transition the decay by electron emission takes place from the initially core-excited state. If the initially excited electron participates in the resonant Auger transition the transition is called a *resonant participator Auger decay* and if not the transition is called a *resonant spectator Auger decay*.

In the fluorescence transition emission of a photon follows the electronic transition and the photon energy of the emitted photon is determined by the energy release of the decaying electronic transition [9].

2.3.3 Core-level photoelectron spectroscopy of metal clusters

In the core-level photoelectron spectroscopy of this work the localized core-level orbitals are probed by soft X-ray radiation [4, 9]. Even for the solid state samples the observed photoelectron spectra plotted as a function of electron binding energy consist of very often separate spectral lines. Moreover, these responses often lack the complex multiplet spectral structure which is characteristic for free atoms of the same material. This is due to the disappearance of the coupling between the core-vacancies and the valence electrons in solids. Clusters have been observed to have similar features to the solid core-level spectra [4]. However, the cluster and solid core-level responses are affected by the probed atoms' local chemical environment which influences the electron binding energy. The binding energy values in metal clusters deviate from both the atomic and solid values. This is due to the various initial and final state effects which have an influence on photoionization process [4]. By analyzing the photoelectron spectra recorded for metal clusters of different sizes, information about these effects and physical properties behind them can be obtained. In this work this approach is used to probe the metallic properties of nanoscale metal clusters.

The environment of a probed atom in metal clusters and solids, which consists of neighbouring atoms and the delocalized valence electrons, affects the energies of the core-level orbitals already before the photoionization takes place and therefore it is often denoted as an initial state effect. After the core-hole has been created in the atom being probed in the cluster, the charge of the core-hole is screened by the valence electrons, and this screening affects the final state energy. Since clusters can be seen as an intermediate state of matter and their properties change as a function of size, the initial and final state effects are not constant but gradually become less prominent for very small clusters and approach solid values for very large clusters.

Since in this work we have studied metallic properties of metal clusters, it is sensible to examine how the core-level energies of clusters change relative

to the corresponding solid values and therefore to define:

$$\Delta E_{bin}^{C-S}(R) = \Delta E_i(R) + \Delta E_f(R), \tag{2.7}$$

where ΔE_{bin}^{C-S} is the binding energy difference between a core-level orbital in a cluster of a radius R and the respective solid, and ΔE_i and ΔE_f are the energy differences of the initial and the final state energies between the metal cluster and the solid, respectively.

Evolution of the initial- and the final-state terms $\Delta E_i(R)$ and $\Delta E_f(R)$ as a function of cluster size has been investigated and disputed for supported clusters in various studies [34–37]. The final state effect has been assigned to be mostly due to electronic relaxation and screening by the valence electrons, while the initial state effects has been suggested to be due to the change in the lattice structure or bonding length with the cluster size, coordination of the atoms in a cluster or the change in the character of the inter-atomic bonding (e.g. from semiconductor to metallic-like). In this work we have assumed that only the final state effects change significantly with the cluster size [38] and therefore in Equation 2.7 the term $\Delta E_i(R) \approx 0$. In this approach the final state effect change is described by a single term $\Delta E_f(R) \propto \frac{1}{R}$ which originates mainly from the Coulombic interaction between the positive charge left on the cluster (assuming clusters are initially neutral) and the outgoing photoelectron in a situation where the screening of the core-level hole is considered to remain solid-like. Another contribution to the $\frac{1}{R}$ term is due to a different work necessary to move the electron over a planar or spherical border of the solid. This model is presented in more detail in Section 2.3.5.

To illustrate a typical core-level photoelectron spectrum of free metal clusters, $4f_{7/2}$ core-level photoelectron spectra for nanoscale bismuth clusters, similar to that in Paper IV, for two cluster sizes are presented in Figure 2.5. In addition to the clusters, Bi atoms and dimers are visible in the spectra due to the cluster production technique in use (see Section 4.3). In the spectra constituents due to different species present in the ionization volume are clearly resolved as separate photolines at different binding energies. Respective binding energy of the $4f_{7/2}$ macroscopic solid is depicted by a vertical bar [39] and the cluster responses are observed at higher binding energies shifted up by ΔE_{bin}^{C-S}.

Since the chemical environment is not the same for different sites in a cluster, separate responses from the each geometric site can be observed in a photoelectron spectrum. Typically for solids only bulk and surface sites differ significantly, and therefore usually two components for each core-level orbital are observed. In clusters, in addition to bulk and surface sites also other sites can be more pronounced, such as in the case of icosahedral geometries (often adopted by free clusters) where atoms residing at the edge or at the vertices of an icosahedron can give different binding energies [4]. In the case of Rb and K clusters, studied in Paper II, separate responses of the bulk and surface atoms

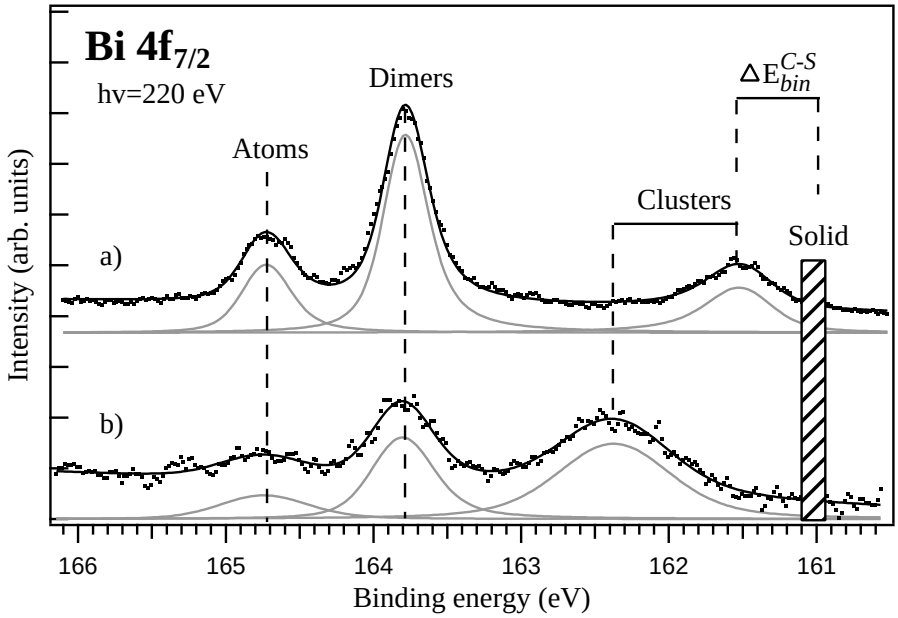

Figure 2.5: $4f_{7/2}$ core-level photoelectron spectrum of nanoscale bismuth clusters for two cluster sizes. Spectrum a) corresponds to the larger clusters and spectrum b) corresponds the smaller clusters. The figure is similar to that in Paper IV.

of the clusters are clearly resolved, and the observed cluster photoelectron spectra are very similar to those of the respective solid. However in the case of Bi, as presented in Paper IV and in Figure 2.5, different geometric sites are not resolved, and this is partly due to the inherent broadening of the photolines, partly due to the broadening caused, for example, by the size distribution of clusters. The magnitude and the sign of the bulk and surface shifts can be estimated using different models considering the initial and final state effects [40–42] or determined experimentally [43].

The bulk and surface components of a cluster photoelectron spectrum have also cluster size dependence, and this has been studied in Paper II. Since small clusters down to sizes of few to few tens of atoms per cluster consist mainly of "surface" atoms the relative intensity of surface components rapidly decreases in the core-level spectrum when size of these smaller clusters becomes larger. Also the relative widths of the surface and bulk components may change as a function of cluster size, as demonstrated in Paper II. This effect may be assigned to the existence of several different kinds of surface states for smaller clusters. The ratio between bulk and surface response intensities has been also used in some previous studies for rare gas and alkali-metal clusters to estimate cluster sizes [44, 45], however in this work this method was not applied.

2.3.4 Valence photoelectron spectrum of metal clusters

The valence photoelectron spectroscopy investigation of free metal clusters' response as a function of cluster size has been carried out in the work described in Papers II-VI. An example of a valence photoelectron spectrum of Bi clusters - similar to that in Paper IV - is shown in Figure 2.6. In contrast to core-level orbitals, valence orbitals of metals are completely or semi-delocalized across the whole cluster volume with valence electrons filling the specific states in the corresponding energy band. Thus a valence photoelectron spectrum consists of multiple responses from each valence state. Due to the delocalization of valence electrons responses of different geometric sites of clusters are not resolved in valence spectra. This is illustrated by Figure 2.6 where a broad and continuous band-like spectrum is observed without any peculiar fine-structure. As in the case of solid metals, at zero temperature the onset of the valence spectrum corresponds the work function of clusters. However, in practice due to the size distribution and non-zero temperatures determining the correct Fermi-level energy from a valence spectrum can be challenging.

Similarly to core-level photoionization, the valence photoionization energy is defined by the initial and the final state. However, the same effects as for the core-level orbitals, such as coordination number, do not have necessarily

as important or any influence on the initial and the final states. In the same way as for the core-levels, the confined positive charge which is left on the cluster after the photoionization, affects the observed binding energy of the photoelectron and gives a cluster size dependency. Thus the similar $\frac{1}{R}$ model as described above for the core-level ionization energies incorporating only this final state effect is also viable for the valence photoelectron spectroscopy.

In Paper II a valence spectrum of large alkali-metal clusters closely resembles the macroscopic solid spectrum with a sharp rise at the Fermi edge while a spectrum of smaller alkali-metal clusters has a more symmetric profile. For Bi clusters in Paper IV no drastic changes in the profile of the valence spectrum have been observed, and in Paper III for Sn clusters the observed responses have been fairly weak and no specific profile has been detected. In Paper V the valence responses of Rb and K clusters have been also simulated using a jellium-based computational model, and in Paper VI an experimental study of the photon energy dependence of Rb valence spectrum along with the computed simulations was carried out. In the first approximation the photoelectron intensity spectral profile of the valence response is mostly defined by the density of states (DOS) at a specific binding energy and the orbital specific cross sections. However, as demonstrated in Papers V and VI for Rb and K clusters, this does not always describe adequately the valence photoelectron spectra.

2.3.5 Conductive sphere approximation

The deviation of the ionization energies of metal clusters from those of the corresponding macroscopic solid can be explained using the so-called conductive sphere approximation (CSA) or, as it is sometimes called, a metal-droplet model [38]. In this model the initially neutral metal cluster is approximated by a conductive metal sphere with a radius R and ionization energy I_C is expressed by the following relation:

$$I_C = W + \frac{e^2}{4\pi\epsilon_0}\frac{\alpha}{R}, \tag{2.8}$$

where W is the work function of the respective planar infinite solid and R is the radius of the cluster. Here the work function corresponds to the ionization energy of an electron at the Fermi-level of the solid metal relative to the vacuum zero level. In the classical theory the constant $\alpha = 1/2$ [38]. However using quantum mechanical corrections somewhat different values for α can be derived [38]. Experimentally different values of α parameter have been observed for different metals. For example, $\alpha = 0.42$ has been determined for some simple metals [38].

The cluster radius is typically expressed as:

$$R = r_s \cdot N^{1/3} + r_0, \tag{2.9}$$

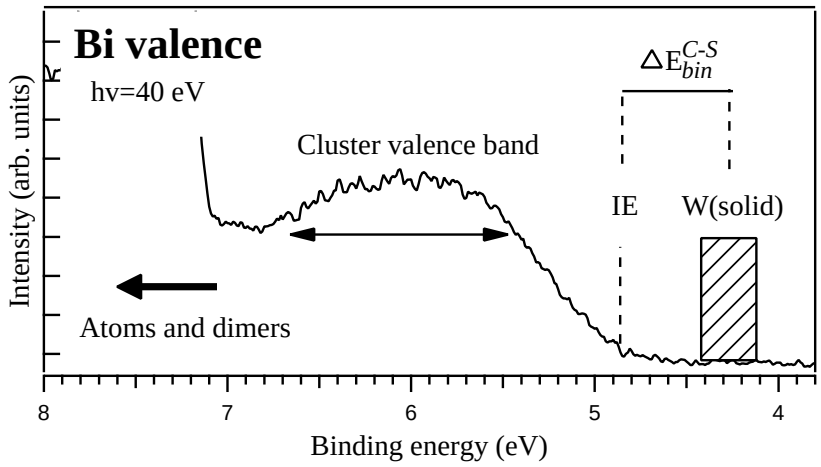

Figure 2.6: Valence photoelectron spectrum of nanoscale bismuth clusters. The valence band is centered around 6 eV. The valence ionization potential is determined from the onset of the valence spectrum and is designated by IE in the figure. Respective work function of 4.27 eV[46] of solid Bi is marked by a vertical bar with the width of the bar corresponding to the estimated error of the value. Cluster-to-solid shift is denoted as ΔE_{bin}^{C-S}. The figure is similar to that in Paper IV.

where N is the cluster size in atoms, r_s is the so-called *Wigner-Seitz radius* describing the atomic density in solid (i.e. volume which a single atom occupies in a solid metal) calculated from the solid density and r_0 is an additional correction term which takes into account the so-called spill-out of valence electron density.

Typically the tabulated values for r_s in many sources do not describe the atomic densities but the densities of the *conduction electrons* (i.e. volume which a single conduction electron occupies) and therefore according to the definition of r_s for electron densities [47, 48], the cluster radius can be expressed as:

$$R = r_s^* \cdot (N_{el} \cdot N)^{1/3} + r_0, \tag{2.10}$$

where r_s^* is Wigner-Seitz radius of the conduction electrons in solid and N_{el} is the number of valence electrons per atom from the viewpoint of the periodic table.

Equation 2.8 can be applied directly in analysis of valence photoelectron spectra, and a similar expression can be also composed for the core-level energy [45]:

$$E_C^{core} = E_\infty^{core} + \frac{e^2}{4\pi\epsilon_0}\frac{\alpha}{R}, \tag{2.11}$$

where E_{∞}^{core} is the core-level ionization energy of the respective solid relative to the vacuum zero level.

Typically the macroscopic solid binding energies are measured relative to the Fermi level E_{∞}^{Fermi} of the metal and therefore work function has to be also taken account:

$$E_C^{core} = (E_{\infty}^{Fermi} + W) + \frac{e^2}{4\pi\epsilon_0}\frac{\alpha}{R}. \tag{2.12}$$

In Papers I-VI equations 2.8, 2.11 and 2.12 have been used to estimate the cluster radii and the cluster sizes from the experimental core-level and valence ionization energies. Typically work functions are not known to a high degree of accuracy introducing an uncertainty to the cluster size estimation.

As mentioned above, responses in the core-level photoelectron spectra are often well resolved narrow lines so the binding energies can be reliably deduced by fitting the core-level spectra. In this sense the latter is better suited for the size estimation than the valence spectra. The obtained binding energies from the core-level studies correspond to the mean size of the clusters in the beam. As explained briefly earlier, determining the ionization threshold from the experimental valence measurements is challenging. Furthermore in this work the onset of the valence spectra corresponds to the clusters with the size higher than the mean size in the distribution.

2.3.6 Line profiles and related effects

An excited state of an atom which decays into energetically lower state has a lifetime τ and an energy release E. According to the Heisenberg's uncertainty principle [49] the uncertainties of lifetime Δt and energy ΔE are connected by the following relation:

$$\Delta E \cdot \Delta t \geq \hbar. \tag{2.13}$$

This relation means that the observed spectral lines in photoelectron spectra are inherently not infinitely narrow but have a so-called *natural linewidth* and that the energy distribution of the photoelectrons follow the *Lorentzian* profile [9]:

$$L(E_0, E) = \frac{\Delta E}{2\pi}\frac{1}{(E - E_0)^2 + (\Delta E/2)^2}, \tag{2.14}$$

where E_0 is the energy value corresponding to the maximum of the profile, ΔE is the profile's full width at half maximum (FWHM), and E - a variable determined relative to E_0.

In contrast to atoms and molecules in a core-level photoionization process of solid metals the ejected photoelectrons may induce electron-hole pairs

near the Fermi-level [50, 51] for what a part of the photoelectron kinetic energy will be lost. As the result an asymmetric tail (towards lower kinetic energies) of the core-level photolines will be observed. The asymmetry can be described using the so-called *asymmetry index* α which depends on the density of states at the Fermi level and degree of the final state screening of the photoionization. A profile of this kind with an asymmetric line shape can be described using *Doniach-Sunjic* formula (DS) [52]:

$$DS(\alpha, E_0, E, \gamma) = \frac{\cos\left[\frac{\pi\alpha}{2} + (1-\alpha)\tan^{-1}\left(\frac{E-E_0}{\gamma}\right)\right]}{[(E-E_0)^2+\gamma^2]^{(1-\alpha)/2}}. \qquad (2.15)$$

Here γ is the half of the photoline's FWHM ($\gamma = \frac{\Delta E}{2}$), E_0 is the energy of the profile's maximum and E is a variable determined relative to E_0. If the asymmetry index $\alpha = 0$ then the profile is equivalent to the Lorentzian function 2.14. The observation of DS-profile bares a witness of metallic properties of the studied clusters [53, 54]. The study of the spectral profiles has been applied in Paper II to probe qualitatively the presence of metallicity in clusters.

In practice the observed line profiles of photoelectron lines are not purely Lorentzian or DS-like but have also contributions from other inherent or external experimental factors which can be typically described or approximated by a *Gaussian* distribution function [9]:

$$G(E_0, E) = e^{-(E-E_0)^2/\delta^2}, \qquad (2.16)$$

where E_0 is the energy of the profile's maximum, E is an energy variable relative to E_0, and $\delta = \frac{1}{2\sqrt{\ln 2}} \cdot \Delta E$. Thus the Lorentzian and DS profiles are typically convoluted by a Gaussian function. In the case of Lorentzian and Gaussian convolution the result is so-called *Voigt* function. Thermal motion of free atoms, molecules and clusters affects the kinetic energies of photoelectrons via *Doppler effect* and in this case the spectral lines are broadened by a Gaussian function [55]. Also in clusters and solids the vibrations of the lattice atoms (phonons) cause line broadening which can be described by a Gaussian profile [51].

2.3.7 Fitting and background analysis

In Papers I, II, and IV fitting has been used to derive spectral characteristics from the experimental photoelectron spectra. In a typical fitting procedure a group of predefined functions are "fitted" with optimizing parameters to the experimental data using least-squares minimization algorithms. Fitting is typically restricted by some a priori known information about the studied system what defines the number of free parameters and enhances the stability and sensibility of the whole process.

One of the most important factors of the fitting and analysis of experimental data in general is the background analysis. The experimental photoelectron spectra do not only incorporate a finite number of well defined photolines but also a continuous background which is induced e.g. by inelastically scattered and secondary electrons. In order to be able to carry out peak fitting the background has to be subtracted or taken into account in the fitting procedure. Thus, always in the fitting some specific profile for the background has to be selected. The most typical background profiles are simple constant or linear profiles, and of Shirley-type [56]. In this work only simple constant and linear background profiles have been used and typically the fitting procedure has been let to optimize the selected background profile to the studied data. In this work the fitting of core-level photolines and background has been carried out using the SPANCF macro package for the Igor Pro software [57].

Chapter 3

Cluster formation

Free clusters can be formed using several different techniques. In this chapter the main cluster formation techniques used in Papers I-VI are presented. In the work reflected in Papers I-VI pick-up and adiabatic expansion processes were used to create metal clusters in the size range from few tens to few hundreds of atoms per cluster.

3.1 Adiabatic expansion sources

An intense beam of atoms, molecules or clusters with specific properties can be created by an adiabatic (isentropic) expansion of gas through a nozzle into vacuum. In this process translational temperature of the expanded medium decreases. At certain temperatures and pressures cluster formation occurs in the vicinity of the exit of the nozzle, creating clusters in the size range of few tens to tens and hundreds of thousands of atoms per cluster. Using an adiabatic expansion source clusters from different kinds of gaseous elements such as rare gases, and from molecular compounds such as H_2O, CO_2, etc. can be produced [58–60].

Since the Ar clusters were used in the experiments of Papers I-VI, in the following sections we mostly review and discuss the main principles of adiabatic expansion and cluster formation in Ar. The treatment follows for some parts the books by H. Pauly [61] and H. Haberland [62] and references therein.

3.1.1 Properties of the adiabatic expansion

In a typical construction of an adiabatic expansion source, gas from a pressurized stagnation reservoir flows through a nozzle into a low pressure (vacuum) expansion chamber. Stagnation conditions can be described by variables of pressure P_0 and temperature T_0. A typical adiabatic expansion set-up used in the works reflected in Papers I-VI is illustrated in Fig 3.1. Expansion pro-

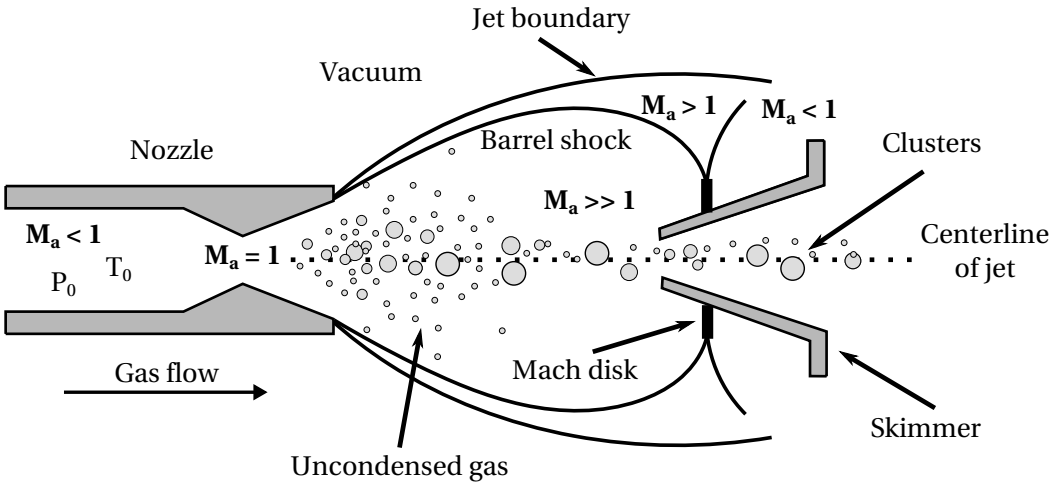

Figure 3.1: Simplified schematic view of an adiabatic expansion via a nozzle into vacuum. Before the expansion the gas flow is described by the stagnation parameters P_0, T_0 and Mach parameter (a ratio of the actual speed to the speed of sound) $M_a < 1$. At the throat of the nozzle the flow is sonic $M_a = 1$ and on the exhaust side of the nozzle the flow becomes supersonic $M_a >> 1$. The most of the condensation and cluster formation occurs at the centerline of the jet up to few nozzle diameters downstream from the nozzle. The particles formed at the centerline are subsequently selected by a conical skimmer.

cess can be described qualitatively by a simple one dimensional treatment which assumes only minor changes in the cross-sectional areas of the flow passage through the nozzle and ideal compressible gas without friction and heat transfer. Since no heat is transferred in the expansion process and entropy is constant on each streamline of the expansion, an adiabatic (isentropic) expansion process is assumed to happen.

For ideal gases the speed of sound, which describes the propagation velocity of a sound wave, is defined as:

$$c = \sqrt{\gamma \frac{RT}{M}}, \tag{3.1}$$

where $\gamma = c_p/c_v$ is gas specific ratio of heats, R is the universal gas constant, T is the absolute temperature of the gas and M molar mass of the gas. For monoatomic ideal gases (e.g. noble gases) $\gamma = 5/3$.

In the gas dynamics, the speed of sound is used often to introduce a relative measure of speed and the velocity of a flow is typically described by the so-called *Mach number*:

$$M_a = \frac{w}{c}, \tag{3.2}$$

which describes the ratio of the flow's velocity w and the local speed of sound c in the gas. Flow is called *subsonic* when $M_a < 1$, *sonic* when $M_a = 1$, and *supersonic* when $M_a > 1$.

The gas flow on the stagnation side has usually relatively low speed - much lower than the local speed of sound in the gas. On the stagnation side the gas is also in thermal equilibrium with the stagnation reservoir which acts as a thermostat for the gas. Sonic velocities can be achieved in the throat of a nozzle, if pressure difference between stagnation conditions and the expansion chamber is adequately high. Note that the term *supersonic* used in the case of gas expansions means supersonic velocity relatively to the *local* speed of sound in the expanded gas. Typical velocities of supersonic jets are not much higher than comparable velocities in traditional effusive vapour sources [61].

In figure 3.2 different kinds of nozzles are illustrated. *Sonic* nozzle consists of only a converging part on the stagnation side and in optimal situation sonic velocities are achieved at the throat of the nozzle. Nozzles consisting of both converging and diverging parts are called *conical* nozzles. Due to historical reasons conical nozzles are sometimes also called *de Laval* nozzles according the Swedish inventor G. de Laval. In a conical nozzle the converging part on the stagnation side acts in a similar way as in the sonic nozzle. However on the exhaust side of the nozzle the diverging part accelerates the sonic beam from the convergent part and forms a supersonic flow ($M_a >> 1$). Furthermore collision rates of gas particles are increased in the conical nozzle which increases efficiency of cluster formation in the expansion process.

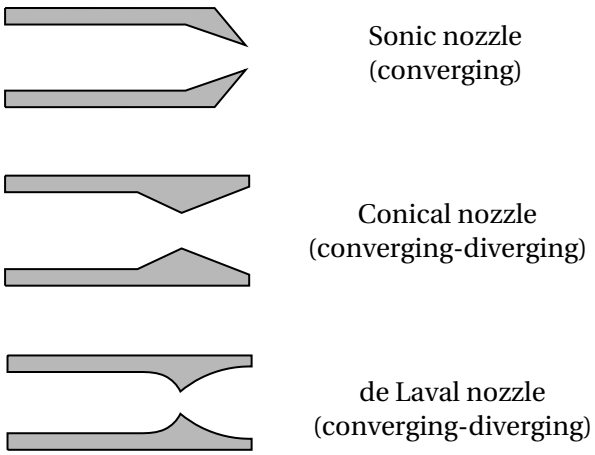

Figure 3.2: Schematic illustration of nozzles with different geometries.

This is especially important feature for photoelectron spectroscopy based on cluster experiments.

3.1.2 Jet profile characteristics

In an adiabatic expansion mechanism the gas is emitted into a conical space angle from the exit of the nozzle, expanding into the surrounding volume. Direction of the flow is however disturbed and turned back into the center of the jet by pressure boundary conditions and shock waves around the expanding gas and compress the jet at the downstream from the nozzle. At this region a so-called *Mach disk* is formed and the pressure of the gas is drastically increased and velocity of jet may reach subsonic values. A simplified example of boundary conditions in a typical expansion process are illustrated in Fig. 3.1. These kind of boundary conditions may affect the formed beam and have to be taken account in design procedure of experimental set-ups. As depicted in Fig. 3.1 it is advantageous to introduce selective skimmer before the Mach disk region to minimize any disturbing effects on the produced cluster beam.

Profile of the expansion flow has been found to be relatively independent of the nozzle geometries [63]. The nozzle geometries are observed to have an effect mostly in the vicinity of the exit of the nozzle in the range of few nozzle orifice diameters. Thus geometry of a nozzle mostly affects processes occurring close to the nozzle exit such as cluster formation.

3.1.3 Cluster formation in the adiabatic expansion

Even though dynamics of adiabatic expansion are well known, no exact models exist for cluster formation and thus in this section only a qualitative description of the cluster formation is given. The cluster formation in adiabatic expansion can be seen as an agglomeration process of individual atoms, dimers or clusters, based on three- and two-body elastic and inelastic collisions.

In the beginning of a cluster formation three-body collisions predominate and individual atoms are nucleated into dimers:

$$3A_1 \rightarrow A_2 + A_1 \qquad \text{dimer formation.} \tag{3.3}$$

The dimer formation requires at least three-body collisions where the additional energy released by the bonding of two gas atoms is transformed into additional kinetic energy of the third not bound atom.

Later when cluster contribution in the jet increases two-body cluster-to-cluster collisions begin to dominate and further cluster growth can be via direct two-body cluster growth between two clusters:

$$A_N + A_M \rightarrow A_{N+M} \qquad \text{cluster growth.} \tag{3.4}$$

Here the energy released in the agglomeration of two clusters increases the temperature of the formed cluster which can be dissipated via several different cluster cooling mechanisms.

These kind of three- and two-body collisions take typically place only in the vicinity of the nozzle exit and at higher distances than few nozzle diameters away the collisions rates may reduce considerably. Due to lack of collisions the formed cluster jet freezes at some point from the nozzle at region which is called sudden freeze or quitting surface. After this surface continuous flow of the gas is changed into free molecular flow and formation of clusters ceases.

3.1.4 Cluster cooling and terminal temperature

Even though translational temperatures of expanded jets may be low, internal vibrational or rotational temperatures of formed clusters might be not. Released energy in the successive cluster growth processes heats up the formed clusters and may lead into substantially higher temperatures than the surrounding expanded gas [64].

In the vicinity of the nozzle exit formed clusters interact with the expanded gas via two- and three-body collisions. If the number of collisions at this region is high enough clusters may achieve thermal equilibrium with the surrounding gas and cool down:

$$A_N + A_1 \rightarrow A_N + A_1 \qquad \text{energy exchange.} \tag{3.5}$$

Alternatively the cluster can also cool down by evaporation of monomers or emission of photons:

$$A_N \rightarrow A_{N-1} + A_1 \qquad \text{evaporation,} \tag{3.6}$$

$$A_N \rightarrow A_N + h\nu \qquad \text{photon emission.} \tag{3.7}$$

These processes are still possible even after the quitting zone, when all other cooling mechanisms have already frozen and the terminal temperature which these cooling mechanisms can achieve depends on the time scale of the experiment.

3.1.5 Cluster size distribution

Due to statistical nature of cluster formation in the adiabatic expansion, a distribution of cluster sizes is formed and typically clusters are designated by the mean size $\langle N \rangle$ of the distribution. Typically size distributions are described by log-normal, linear-exponential or Gaussian profiles and profiles are observed to be depending on the expansion conditions [60–62, 65]. Distribution profiles are relatively broad and usually have values close to the mean size of the distribution [65, 66].

3.1.6 Scaling laws - semi-empirical approach to determine cluster sizes

Since no exact models of cluster formation in the adiabatic expansion exist, semi-empirical *scaling laws* have been derived [67–70]. Formulation of the scaling laws allows comparison of different kinds of expansion conditions and estimation of cluster sizes. In this framework the expansion process and the subsequent cluster formation can be described by a single Γ^* parameter, introduced by Hagena [69, 70]. Because the cluster size is completely determined by Γ^*, equal values of Γ^* for different expansion conditions yield always the same cluster size. This relation makes it possible to change some parameters of the expansion while still produce similar cluster sizes - if the value of Γ^* remains the same.

Small values of Γ^* has not been observed experimentally to induce any clustering of the expanded gas. Only in conditions where $\Gamma^* > 200 - 1000$ some clustering occurs [69]. Dependence of clustering from the Γ^* parameter is characterized below:

No clusters	$0 < \Gamma^* \leq 200$
Transition region with some clustering	$200 < \Gamma^* \leq 1000$
Intensive clustering, $\langle N \rangle \approx 100$	$\Gamma^* > 1000.$

	He	Ne	Ar	Kr	Xe	H_2	D_2	N_2	O_2	CO_2	CH_4
K_{ch}	3.85	185	1646	2980	5554	184	181	528	1400	3660	2360

Table 3.1: Characteristic constants K_{ch} for various gases from Ref. [71] and [72].

In the Γ^* formalism the expansion is determined completely from the initial stagnation conditions (P_0, T_0) of the expansion, geometrical parameters of the nozzle, and the characteristic parameter of the expanded gas. Using these variables the Γ^* can be expressed as:

$$\Gamma^* = K_{ch} \left(P_0 d_{eq}^q T_0^{0.25q-2.5} \right), \tag{3.8}$$

where K_{ch} $[K^{2.5-0.25q} mbar^{-1} \mu m^{-1}]$ represents the gas specific constant, P_0 $[mbar]$ stagnation pressure, T_0 $[K]$ stagnation temperature, d_{eq} $[\mu m]$ effective diameter of the nozzle, and q is an experimentally determined parameter. Values for the q parameter have to be determined experimentally and $0.5 < q \leq 1.0$. For values $\Gamma^* < 10^4$, the value $q = 0.85$ has been proposed [66, 70] and is commonly used. Values for the constant K_{ch} for various gases in the case of $q = 0.85$ are presented in Table 3.1.

In the case of a conical nozzle the equal diameter of a nozzle d_{eq} can be expressed as:

$$d_{eq} = 0.74 \frac{d}{\tan \alpha}, \tag{3.9}$$

where d $[\mu m]$ is the diameter of the nozzle's throat orifice and α is the half-opening angle of the diverging part of the conical nozzle (2α = total opening angle).

Several formulae has been proposed for the mean cluster size $\langle N \rangle$ as function of the Γ^* parameter. Relation for the $\langle N \rangle$ has been observed to be different for the different Γ^* regimes and below relations for the mean cluster size $\langle N \rangle$ for different values of the Γ^* are presented from Refs. [66, 73].

$$\langle N \rangle = 38.4 \left(\frac{\Gamma^*}{1000} \right)^{1.64} \qquad 350 \leq \Gamma^* \leq 1800 \tag{3.10}$$

$$\langle N \rangle = 33 \left(\frac{\Gamma^*}{1000} \right)^{2.35} \qquad 1800 < \Gamma^* \leq 10^4 \tag{3.11}$$

$$\langle N \rangle = 100 \left(\frac{\Gamma^*}{1000} \right)^{1.8} \qquad \Gamma^* > 10^4 \ . \tag{3.12}$$

Equation 3.10 is the original relation suggested by Hagena [70]. For the case $\Gamma^* > 1800$ Buck et al. [66] have also proposed alternative relations for the conical nozzles.

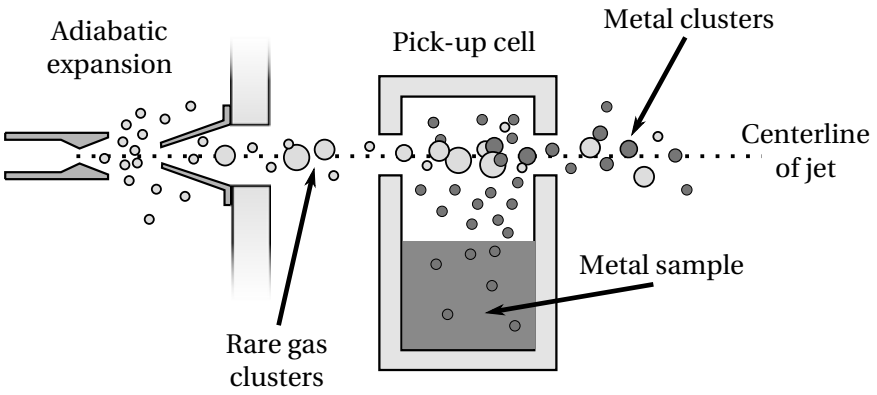

Figure 3.3: Schematic view of a pick-up process.

3.2 Pick-up technique

An adiabatic expansion cluster source can be used in combination with the so-called pick-up technique - in order to form an intense beam of metal (or other parent solid materials) clusters containing from few atoms to few hundreds of atoms. The resulting cluster-production process utilizes agglomeration of guest atoms or molecules picked up by large host clusters [65, 74, 75]. In this section we mostly examine the pick-up of metal atoms and their subsequent cluster formation on host Ar rare gas clusters.

3.2.1 Properties of pick-up mechanism and cluster formation

In a typical pick-up set-up - illustrated in Fig. 3.3 - rare gas clusters produced by the supersonic expansion are guided through a pick-up cell - usually an oven or a gas cell - in which vapour of monomers are picked up and captured by the host clusters acting as a cold thermal reservoir for the captured constituents. Successively picked up and cooled down monomers agglomerate and form guest clusters at the surface or inside of the rare cluster [65].

Additional energy released in the capture and coagulation processes of guest monomers is dissipated by evaporation of the rare gas cluster atoms resulting in shrinkage of the rare gas cluster [65, 76, 77]. For a macroscopic solid metal the cohesive energy of an atom is typically in the range of $1 - 5$ eV [12], whereas for Ar atoms the cohesive energy of a rare gas atom is about 100 meV [12]. Thus as a rule of thumb estimate of the dissipation efficiency can be as follows: 1 eV of released energy may lead into evaporation of approximately 10 Ar atoms.

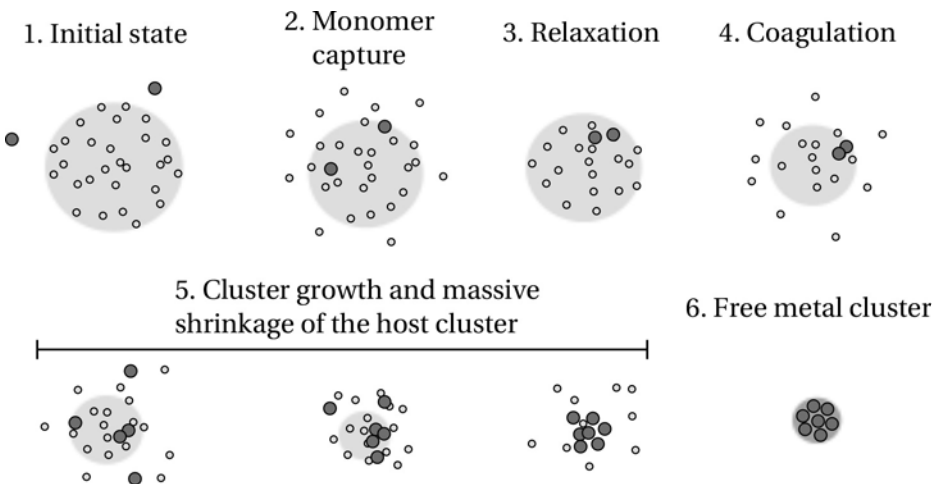

Figure 3.4: Formation of free and pure metal clusters in a pick-up process. Guest metal atoms are captured and coagulated until the host rare gas cluster is completely evaporated.

3.2.2 Formation of mixed and pure guest clusters

If only few pick-up collisions occur and shrinkage of the host cluster has not led to its disintegration a mixed guest-host cluster can be formed, and the guest cluster may locate at the surface or inside of the host cluster [65, 76–88].

Massive coagulation of guest atoms may lead to complete evaporation of surrounding host-cluster atoms and formation of a pure guest cluster [76, 77, 85, 88]. Stepwise formation of pure metal clusters via the pick-up technique in the case of complete host cluster evaporation is schematically depicted in Fig. 3.4. This condition can be achieved by high pick-up cell pressures, which are typically in the range of $10^{-3} - 10^{-2}$ mbar [76, 77, 85, 88].

In this work the cluster source has been operated at such conditions where the production of pure metal clusters was expected [88]. Furthermore due to the weak interaction between metal atoms and rare gas atoms the effect of rare gas environment may also be negligible for the study by photoelectron spectroscopy.

3.2.3 Terminal temperature of the guest clusters

Pick-up and agglomeration of metal clusters occurs only inside the pick-up cell, as depicted in Fig. 3.3. After this region, in the case of mixed metal-rare gas clusters no additional heat is brought into the rare gas cluster and evaporation of rare gas atoms continues as long as the system reaches thermal equilibrium. In this state the system - including the guest cluster - typically approaches terminal evaporational temperature of the rare gas cluster. In

the case of doped Ar clusters temperatures down to approximately 30 K have been observed [89].

In the case of pure metal clusters where all the rare gas atoms have been evaporated, determination of the terminal temperature is difficult. Since the dissipation of energy via rare gas evaporation is not possible anymore the terminal temperature of a metal cluster may be, in principle, drastically higher than the temperature of a mixed rare gas cluster in an equilibrium state.

3.2.4 Cluster size distribution

As in the case of cluster formation in adiabatic expansion, formation of clusters using the pick-up technique is a statistical process and formed metal clusters have a distribution of sizes. In a simple case where interaction with the guest particles can be treated as a process of independent collisions with the cross-sections for the pick-up procedure being invariant Poissonian statistics is valid and Poissonian shaped cluster size distribution is expected [90]. However, strong deviations from the Poissonian profiles can be observed due to the shrinkage of the host rare gas cluster and the influence of the initial size distribution of the rare gas clusters. [91, 92].

Chapter 4

Experiments and instrumentation

4.1 Storage rings and synchrotron radiation

At a synchrotron electromagnetic radiation is created when charged particles, typically electrons, are kept on a circular-like path by strong magnetic fields and the charged particles experience a centripetal acceleration [93, 94]. The modern 3rd generation synchrotron storage rings are viable tools for many fields of physics, since high flux of radiation and tunability of the radiation energy in a wide range from vacuum ultraviolet light to hard X-rays [94]. Furthermore, the polarization properties are also well defined.

In this work all the experiments have been carried out using soft X-ray synchrotron radiation at the synchrotron radiation facility MAX IV laboratory.

4.1.1 The main principles of synchrotron radiation

In a typical synchrotron storage ring a beam of electron bunches moves at relativistic velocities ($v \approx c$) inside the circular-like vacuum chamber. Usually the electron beam is injected to the storage ring from an external source, and the function of the storage ring is to keep this electron beam stable in dimensions and not loosing the current inside the ring for as long time as possible.

Electric and magnetic fields force electrons to change their trajectory under the so-called *Lorentz force*:

$$\mathbf{F} = q(\mathbf{E} + \mathbf{v} \times \mathbf{B}), \tag{4.1}$$

where $q = -e$ is the charge of an electron, is $\mathbf{v}$ is the velocity vector of an electron, $\mathbf{E}$ is the electric field vector, and $\mathbf{B}$ is the applied external magnetic field. This equation shows that if electrons are moving at relativistic velocities

magnetic fields can cause much stronger force than static electric fields. Thus in a storage ring magnetic fields are used to control the moving electrons.

Some of the most important parts of the ring are *bending magnets* in the junctions of the straight sections of the ring and the so-called *insertion devices*, such as *wigglers* and *undulators*, located at the straight sections of the ring. The purpose of the bending magnets is to deflect the electron beam and to ensure that the beam stays on the correct path, inside the ring. Since the electrons experience centripetal acceleration inside the bending magnets, synchrotron radiation is created at that point and this kind of radiation is so-called *bending magnet radiation*. The energy profile of bending magnet radiation is typically very broad and continuous.

Wigglers and undulators consist of a periodic array of magnets so they can be characterised by a dimensionless parameter:

$$K = \frac{eB\lambda_u}{2\pi m_e c}, \tag{4.2}$$

where B is the strength of magnetic field between the magnet arrays and λ_u is the period of the magnets, e is the elementary charge, m_e is the mass of an electron, and c is the speed of light. For wigglers $K \gg 1$ and undulators $K \approx 1$.

In a wiggler the produced radiation is continuous and similar to the bending magnet radiation. However, the radiation from a wiggler has much higher flux than from a bending magnet (intensity $\propto 2N$, where N is the number of magnets in a wiggler).

Undulators do not generate a continuous and broad profile of photon energies but a discrete spectrum with intensity maxima at specific energies [94]:

$$\lambda_n = \frac{\lambda_u}{2n\gamma^2}\left(1 + \frac{K^2}{2} + \gamma^2\theta^2\right), \tag{4.3}$$

where n is a positive integer, a so-called harmonic number. Intensity of these maxima is much higher than the radiation from bending magnets or wigglers (intensity $\propto N^2$).

In addition a storage ring contains quadrupole magnets to focus the electron beam and RF-cavities to maintain the energy of the electrons, which is partially lost due to the emission of synchrotron radiation in the bending magnets and in the insertion devices.

4.1.2 MAX-IV laboratory: Beamline I411

Soft X-ray beamline I411 is located at 1.5 GeV MAX-II storage ring, at MAX IV laboratory, in Sweden [95, 96][1]. The beamline is designed for gas and

[1]For more information see: www.maxlab.lu.se

solid phase measurements, and a differential pumping stage in front of the end-station makes it possible to carry out experiments at low high-vacuum conditions. The linearly and horizontally polarized synchrotron radiation is produced by a 2.65 m long 87-pole undulator with a maximum $K = 3.6$ value. The distance between the magnetic arrays (gap) can be adjusted from 20 mm to 300 mm.

The synchrotron radiation coming out from the undulator is focused to a modified SX-700 plane grating monochromator by spherical mirror, and from the monochromator the beam is focused by a plane elliptical mirror to an exit-slit where a slice of the beam is selected and the monochromatization of the beam is realized. The synchrotron radiation coming out from the exit slit is focused by a torroidal mirror, into a permanent end-station, located at the end of the beamline [97]. Currently the photon energy range of the beamline is from 40 eV to 1500 eV and the resolving power is about $6 \cdot 10^3$. Spot size of the synchrotron radiation beam at the end-station is horizontally approximately 0.5 mm and vertically around 1.0 mm, depending on the applied monochromator settings [95]. A typical photon flux obtained at I411 is in range of $10^{11} - 10^{13}$ photons/s/100 mA/0.1% BW at the experiment [95].

4.2 Electron energy analyzers

Intensity distribution of electrons as a function of their kinetic energy can be determined by electrostatic electron energy analyzers. In this work a *hemispherical* electron analyzer has been used in which the electrons travel between the inner and outer hemispheres on a circular path in a static electric field. The electric field induces a Lorentz force, according to Equation 4.1, and the radius of the electrons' flight path depends on their initial kinetic energy. The kinetic energy which is required from the electrons to stay on the centre path is the so-called *pass energy*. The pass energy is kept constant and in a certain measurements the electrons are retarded and focused by an electrostatic lens before entering the electric field of the hemispherical electrodes. In this way the energy of the electrons ejected by the sample can be scanned and a photoelectron spectrum over a chosen energy range can be acquired. A schematic presentation of a typical hemispherical analyzer is shown in Figure 4.1. The electrons which reach the end of the hemispherical electrodes are registered typically by a detector incorporating MCP plates and a CCD camera or by the so-called resistive anode detectors.

Base-resolution of a hemispherical analyzer can be defined as:

$$\Delta E = \frac{d}{2R} E_{pass}, \tag{4.4}$$

where d is the size of the entrance slit, R is the radius of the centre circular path in the analyzer and E_{pass} is the pass energy.

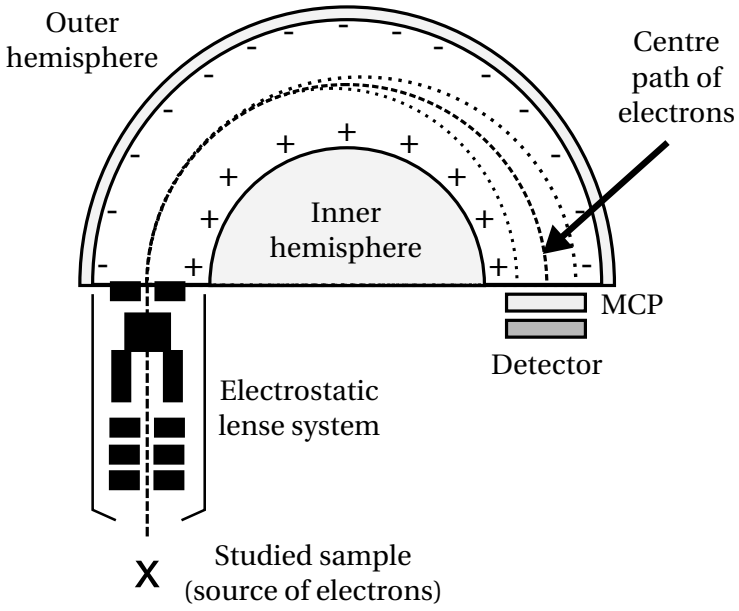

Figure 4.1: Schematic illustration of a typical hemispherical electron energy analyzer.

If the photon energy of the used exciting radiation is known then the photoelectrons and their photoelectron spectrum can be described by a binding energy scale using the following relation:

$$E_{bin} = h\nu - E_{kin}, \tag{4.5}$$

where $h\nu$ is the photon energy of the exciting radiation and E_{kin} is the kinetic energy of the studied electrons.

Photoelectron spectroscopy measurements are in practice always a trade-off between the signal intensity and the spectral resolution. In the experiments of this work, the applied experimental settings of the analyzer and the beamline are typically chosen to match the experimental broadening to the widths of the studied spectral structures.

4.2.1 Scienta R4000

In this work a hemispherical Scienta R4000[2] spectrometer located at the permanent end-station of beamline I411 was used to record the photoelectron spectra. The R4000 spectrometer has a circular flight path with a radius of $R = 200$ mm and the electrons are detected by a CCD detector. The spectrometer is installed at the beamline in such a way that the observation

[2]For more information see: www.vgscienta.com

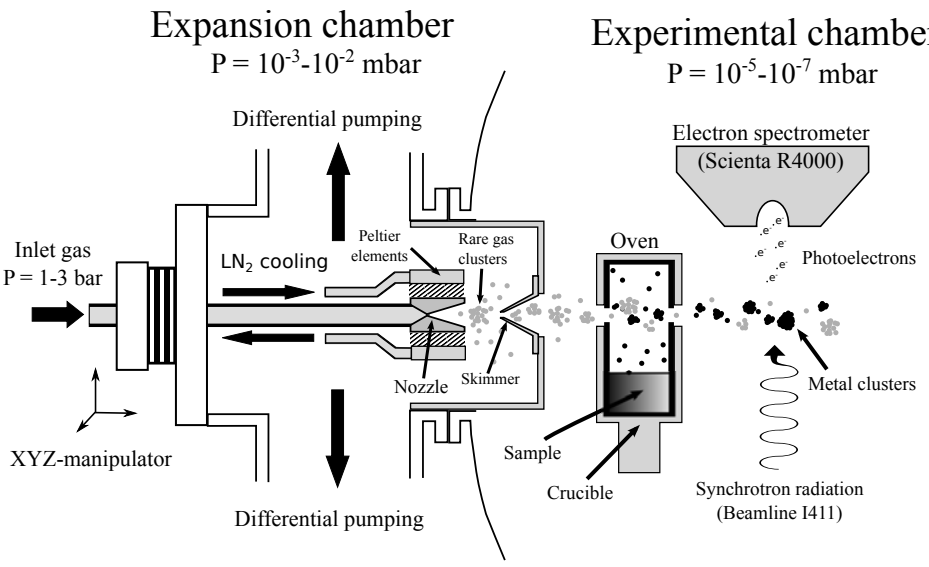

Figure 4.2: Schematic view of the EXMEC set-up.

angle relative to the synchrotron radiation polarization can be adjusted and in this work the spectra were collected either at 90° or at the "magic" 54.7° angle.

4.3 Exchange Metal Cluster Source (EXMEC)

In this work the metal clusters have been formed by a pick-up technique implemented in the so-called *Exchange Metal Cluster Source* (EXMEC), capable of producing free, pure and neutral metal clusters from various metallic elements. The EXMEC set-up consists of two main sections: a rare gas cluster source based on the adiabatic expansion and a pick-up cell where the metal sample is evaporated and rare gas clusters interact with metal vapour. A schematic view of the EXMEC set-up is shown in Figure 4.2 and its more detailed presentation is given in Paper I.

As described earlier, in the rare gas cluster source Ar clusters are formed by expansion of pressurized Ar gas via a conical stainless steel nozzle which is mounted on a XYZ-manipulator for aligning purposes. The nozzle has a fixed orifice of 150 μm and the divergent cone at the vacuum side is 20 mm long and has a 10° total opening angle. The temperature of the nozzle can be varied using Peltier elements and a liquid agent cooling arrangement mounted directly on the nozzle's copper housing. Typically in the experi-

ments the nozzle was cooled down by a liquid nitrogen circulation and the final temperature of the nozzle was adjusted by the Peltier elements. Furthermore, in addition to the liquid nitrogen cooling, also an in-house developed liquid-glycol cooling device was used to control the nozzle temperature. This arrangement as a whole (with different cooling agents) provides a wide adjustable range of nozzle temperatures from room temperature down to the temperature of -196 °C of liquid nitrogen.

The rare gas expansion chamber is pumped by two horizontally mounted turbo pumps with a pumping speed of 1000 l/s per pump and at typical operating conditions in the expansion chamber the pressure is in the range of 10^{-3} to 10^{-2} mbar. The produced Ar jet containing Ar clusters and Ar atoms comes through a conical copper skimmer (orifice diameter 500 μm) which is located downstream from the nozzle. The distance between the skimmer and the nozzle can be adjusted by the XYZ-manipulator.

The skimmer also separates the expansion chamber from the experimental (ionization) chamber where the pick-up cell is located and the cluster jet is crossed by the X-ray photon beam. The experimental chamber is typically kept at the pressure of $10^{-5} - 10^{-7}$ mbar, depending on the operating parameters of the EXMEC set-up. In this work the pick-up cell with two horizontal orifices was made compatible with the Scienta R4000 electron analyzer mounted on the experimental chamber. The pick-up cell consists of a stainless steel or a molybdenum crucible which is heated by either resistive heating (based on the absorption of thermal radiation) or induction heating (based on induction of eddy currents on the crucible and metallic sample by fluctuating magnetic fields) [98]. In Papers I-II and IV-VI Rb, K and Bi samples were evaporated using resistive heating, while in Papers I and III Sn sample was evaporated by induction heating. The use of resistive and induction heating allows to cover a wide range of temperatures from room temperature up to 2000 °C and thus makes it viable to evaporate a wide range of low and high vapour pressure elements.

As explained in Section 3.2, inside of the pick-up cell metal atoms are picked-up by Ar clusters and metal clusters are gradually formed via the pick-up procedure. In this work the estimated metal vapour pressure inside of the crucible was in the range of $10^{-2} - 10^{-3}$ mbar what is expected to provide high doping rate of the Ar clusters and ensure production of pure metal clusters [88]. As again discussed in Section 3.2, due to the nature of the cluster formation mechanism a distribution of metal cluster sizes is produced with the mean size of the distribution possible to control by varying the main parameters of the EXMEC set-up: Ar cluster size and the oven pressure.

Chapter 5

Summary and discussion of the included papers

5.1 Experimental set-up for electron spectroscopy based cluster research (Paper I)

In Paper I technical design of the EXMEC set-up and first results on Rb and Sn clusters are presented. The aim of this work has been to develop the first version of the EXMEC set-up and to show its capability to produce clusters in the size regime of few tens to few hundreds of atoms per cluster. Moreover the set-up was found to be capable to produce clusters from high and low vapour pressure metals using two kinds of evaporation techniques: High vapour pressure Rb was evaporated using resistively heated oven while low vapour pressure Sn was evaporated using induction heating.

Core-level photoelectron spectroscopy has been used to investigate the electronic structure of Rb and Sn clusters. Photoelectron spectra of Rb $4p_{1/2}$ and Sn $4d_{5/2,3/2}$ have been recorded and properties of clusters have been determined by spectral analysis. Four different experimental conditions each creating Rb clusters of a certain size are presented in Paper I. For Sn a spectrum for one size of clusters is presented. Core electron spectra have been used to determine the mean sizes of the produced clusters using the CSA-model, presented in Section 2.3.5. The sizes of Rb clusters have been estimated to be in the range of $\langle N \rangle \approx 60 - 220$. Mean size of Sn clusters have been estimated to be approximately ≈ 200 atoms. The Ar cluster sizes used in the experiments or Rb, have been estimated using the similar scaling law approach as presented in Section 3.1.6, with a cluster size range from 1400 to 25700 atoms per cluster.

The first results, presented in Paper I have demonstrated the capabilities of the EXMEC set-up for photoelectron spectroscopic studies. In later works some modifications and enhancements were made to the set-up to enhance

the operational stability but for the larger part the set-up has remained the same. The development of the EXMEC set-up has provided also a solid foundation for further cluster research of metal and molecular clusters presented in Papers B-F.

5.2 Study of metallic clusters using photoelectron spectroscopy (Papers II-VI)

In Papers II-VI core-level and valence photoelectron spectroscopy has been used to investigate the evolution of metallic properties of free, neutral and size varied nanoscale Rb, K, Sn, and Bi metal clusters.

5.2.1 Core-level photoelectron spectroscopy of clusters

In Paper II a more thorough investigation of Rb clusters has been presented, as well as a study of K clusters. 4p core-level spectra have been recorded for four Rb cluster sizes: $\langle N_{Rb} \rangle = 40, 90, 110, 170$ and 3p core-level spectra for two K cluster sizes: $\langle N_K \rangle = 90, 650$. In Paper III 4d core-level photoelectron spectroscopy has been used to study Sn clusters in detail presenting the spectra for four Sn cluster sizes: $\langle N_{Sn} \rangle = 40, 60, 200, 500$. Size of Ar clusters in the Sn experiments have been also estimated to be in the size range from 400 to 140000 atoms per cluster. In Paper IV 4f and 5d core-level photoelectron spectroscopic investigation of Bi clusters has been performed presenting spectra for seven cluster sizes: $\langle N_{Bi} \rangle = 20, 30, 50, 60, 80, 150, 330$.

In each work for the largest clusters of the series cluster-to-solid binding energy shifts are observed to be rather small, suggesting metallic properties at least for the largest studied clusters. Furthermore, for each metal except for Sn, the evolution of the cluster-to-solid shift has been smooth and monotonous indicating no drastic changes in the properties of the clusters and therefore suggesting metallic properties for all cluster sizes, except for the smallest Sn clusters. In the case of the smallest Sn clusters ($N \approx 40$), in Paper III, an additional spectral feature appearing in the $4d$ core-level spectrum is proposed to be due to the non-metallic phase of Sn clusters. For such non-metallic energy structure the final state screening can decrease remarkably and thus the cluster features are expected at different binding energies in spectra relative to metallic Sn clusters of a similar size. This idea is supported by an earlier study on anionic Sn clusters, where semiconductor-to-metal transition has been observed close to cluster size $\langle N_{Sn} \rangle = 40$ [30].

Similarly to Paper I, in Papers II-VI the cluster sizes have been estimated using the CSA-model and the core-level binding energies determined in the experiments. In Papers II, III, V and VI the cluster size estimations have had to involve the macroscopic solid work functions known with a limited

accuracy. In Paper IV the core-level solid energies measured directly relative to the vacuum level in Ref. [39] have been used.

In Paper II each of the $4p_{1/2}$ and $4p_{3/2}$ core-level photolines of Rb clusters is split into two sub-components due to bulk and surface states. In the case of K clusters' study, presented in Paper II, separate bulk and surface components have not been resolved, partly due to the inherent line width of the K $3p_{1/2}$ and $3p_{3/2}$. Similarly in Papers III and IV for Sn and Bi clusters bulk and surface states have not been resolved due to the widths of the core-level photolines.

Since intensity (total area) of bulk and surface components of cluster responses depends on the number of bulk and surface atoms the ratio between the components provides additional information on the size and geometric structure. In the case of Rb clusters (Paper II) the bulk-to-surface ratio has been observed to decrease rapidly as a function of cluster size. This indicates that the size of the clusters is in the regime where surface atoms are in majority, suggesting size range of few tens to few hundreds atoms.

In Papers II and IV the width of the core-level cluster responses has been observed to increase with the decreasing cluster size. Since the EXMEC set-up produces a distribution of sizes and because the binding energy difference becomes larger for smaller sizes, some broadening of the core-level lines can be expected with the decreasing cluster size. However, for Rb and K clusters (Paper II) the widths of the bulk components are observed to increase only slightly when the surface components increase drastically. This difference in spectral changes with the size is proposed to be due to the increased number of different surface sites for the smallest cluster sizes. In the case of Bi clusters (Paper IV), the bulk and surface components are not resolved and therefore only an increase in the overall widths of the cluster responses is observed at smaller sizes.

As described above, to determine spectral characteristics of core-level photolines least-square fitting has been used. In Papers II and IV the spectral characteristics of Rb, K and Bi clusters have been determined by fitting using Igor Pro macro package SPANCF [57]. In our spectra cluster features consist of multiple photolines due to all the clusters in the size distribution. However because of the inherent line widths and of the limited experimental resolution separate peaks for each cluster size are not resolved. Thus single lines for each spin-orbit or bulk/surface component have been used. To address the question whether small Rb and K clusters are metallic, different spectral profiles for the Rb $4p$ and K $3p$ responses, among them Doniach-Sunjic profile, have been tested in the data handling of Paper II. It has been found that Doniach-Sunjic spectral shapes with the solid Rb and K asymmetry indices gave the best description of the clusters responses and this suggests metallicity of the studied Rb and K clusters. In the study of Bi clusters presented in Paper IV, asymmetric line profiles have not been ob-

served and therefore for simplicity the cluster responses have been fitted with Voigt profiles. In Paper III presenting the results on Sn clusters, the binding energy values of Sn $4d_{5/2}$ and $4d_{3/2}$ cluster responses have been determined using the centre-of-gravity positions of the peaks instead of fitting.

In solid state a Bi crystal has a poorly conductive bulk and a well conductive surface, and this special property has been a topic of studies related to nanoelectronics and topological-insulators [99–107]. In Paper IV we have studied how this surface conductivity scales down to nanoscale clusters. In solid the conductive surface states may penetrate in to the bulk and this addresses a question whether the nanoscale Bi clusters are completely non-metallic or metallic, or have a heterogeneous structure consisting of a poorly conductive bulk and a highly metallic surface. For nanoscale Bi ensembles the MIT has been proposed but not unambiguously verified [107, 108] and a phase transition of crystal structure from well defined lattice symmetries to amorphous features has been suggested to happen in supported Bi granules at dimensions close to 4 nm [106]. The experimental core-level spectra of Bi do not indicate any resolvable components due to the metallic and non-metallic phases of Bi and therefore the core-level analysis suggests homogenous Bi clusters across the whole cluster size range $N = 20 - 330$ ($\mathrm{R} = 0.5 - 1.4$ nm), which is well below the dimensions of 4 nm.

5.2.2 Valence photoelectron spectroscopy of clusters

Valence photoelectron spectra of Rb, K, Sn and Bi clusters have been recorded for the same clustering conditions as the core-level spectra in Papers II-IV. In Paper VI the valence spectra of Rb clusters were recorded for several photon energies and a single cluster size. The valence responses have been observed at higher binding energies than the corresponding solid work-functions and posed similar cluster size dependence as the core-level features.

In Paper II the valence spectra have been recorded for two cluster sizes: $\langle N_{Rb} \rangle = 40, 170$ and $\langle N_K \rangle = 90, 650$, respectively which correspond to the smallest and the largest cluster sizes in the series with the core-level spectra. For the largest Rb and K clusters the profiles of the valence responses have been observed to be solid-like with a Fermi-edge type of a steep flank, while for the smallest clusters the valence responses have more smooth symmetric shapes. Noticeable changes in the shape of the valence spectrum - in addition to the cluster size dependent binding energy shift - indicates substantial change in the DOS structure between the larger and the smaller sizes. Change of DOS from a solid-like response to something drastically different is an expected feature for clusters with a size in the range of few tens to few hundreds atoms an thus the experimental valence spectra of Rb and K clusters support the core-level analysis which indicated metallic properties.

For Sn clusters (Paper III) the valence spectra have been recorded for

three cluster sizes: $\langle N_{Sn} \rangle = 60, 200, 500$. Due to weak valence responses the valence spectrum has not been recorded for the smallest $\langle N_{Sn} \rangle = 40$ clusters. Thus possible changes in the valence spectra corresponding to the additional feature observed in the core-level spectra could not be investigated.

For Bi clusters (Paper IV) the valence spectra have been recorded for seven cluster sizes: $\langle N_{Bi} \rangle = 20, 30, 50, 60, 80, 150, 330$. The valence responses have been observed to be remain quite similar through the whole size range and only size dependent shifting and some change in the width of the cluster responses has been observed. The latter has been proposed to be due decreased coordination as a function of decreasing cluster size. In addition to this, there may also be changes in the spectra due to a change in the DOS. Additional fine-structure is not observed in the valence spectra of Bi clusters and the cluster responses resemble smooth profiles observed for the poly-crystalline Bi [109]. Solid-like surface responses [110] were not expected to be observed, due to absence of fixed geometry in the experiments. Thus valence spectra do not indicate any proof of heterogenous Bi clusters - with conductive surface and non-metallic bulk - and therefore the results of the valence analysis are consistent with the core-level investigation.

In Paper II on Rb and K clusters the valence onsets have been determined and the cluster-to-solid binding energy shifts have been found to be close to the corresponding core-level values, even though somewhat smaller. Thus the cluster size estimations from the valence spectra yields larger cluster sizes than the core-level treatment. However, due to the size distribution of the studied metal clusters and the fact that the lower binding energy side of the valence profile gets most from the largest clusters, the smaller cluster-to-solid binding energy shifts in valence relative to core-levels have been proposed to be due to the cluster size distribution. Therefore the results of the valence analysis are consistent with that of the core-level. For Sn and Bi clusters (Papers III and IV), the valence onsets have not been determined but the core-level cluster-to-solid shifts have been added to the solid work-functions. Similarly to Rb and K clusters, the core-level cluster-to-solid shifts of Sn and Bi correspond relatively well to the valence shifts when the uncertainties in the determined cluster and reference solid values are taken into account.

The determination of the Fermi-edge is also challenged by the change of the DOS (i.e. shape of the valence response), as observed for Rb and K clusters. The change of the DOS has been studied in Paper V, in which the jellium model simulated valence spectra have been compared with the experimental ones for Rb and K clusters, presented in Paper II. The estimated mean cluster sizes, in Paper V, were $\langle N_{Rb} \rangle = 50, 200$ for Rb and $\langle N_K \rangle = 30, 650$ for K, and the jellium-simulations have been carried out for electronic-shell magic numbers close to the estimated experimental cluster sizes. Spectra of the Rb clusters have been simulated using cluster the sizes: 58 and 198. Spectra of the smallest K clusters have been simulated using

the two cluster sizes 34 and 40 in order to get a better agreement with the experimental spectra for which a distribution of sizes exists. The larger K cluster spectra have been simulated for a single size of 676. In order to evaluate the effect of the continuum wave functions for the cross sections of the valence ionization transition every simulation was carried out using two approaches: 1) a description where the valence responses are determined only by the electron occupation of the jellium orbitals (i.e. DOS description) and 2) where the continuum wave functions for the final ionized states are taken into account in the cross sections. While the first approach provides a reasonable description with some deviation of the calculated spectral overall shape from the experiment, the inclusion of continuum wave functions enhances the description remarkably. The simulation confirms that the changes in the valence photoelectron spectra are indeed due to the change of the DOS and therefore the valence spectra are not well suited for performing cluster size estimations using the CSA-model.

In Paper VI the valence spectra of Rb clusters have been studied as a function of photon energy and the experimental valence spectra have been recorded for a single mean cluster size of $\langle N_{Rb} \rangle \approx 90 \pm 20$ and for three photon energies: 40.2, 48.8 and 58.6 eV. In the valence band region ($2.4 - 3.6$ eV) the relative intensities of the experimental cluster responses have been observed to change as a function of photon energy and these oscillations have been described by the jellium model simulations - similar to those of Paper V - with the continuum wave functions for the final states. In order to take into account the cluster size distribution the simulations have been carried out for several cluster sizes $N = 90 \pm 10$ with a Gaussian weight and FWHM of 12 atoms. The simulations suggest that the intensity deviations of the experimental valence spectra are due to the photon energy dependent cross section oscillations of the 1h, 2d, 1g, and 2p jellium-orbitals. This kind of behaviour has been predicted previously for Na clusters [111] and it is verified by the experimental and theoretical results of Paper VI.

Chapter 6

Conclusion and outlook

Synchrotron radiation excited core-level and valence photoelectron spectroscopy has been used to study electronic properties of free, neutral and size varied metal clusters in nanoscale dimensions using the EXMEC set-up. In this work we reported experimental results of K, Rb, Sn and Bi clusters which indicated metallic properties for the cluster size range from few tens to few hundreds atoms per cluster and only for Sn clusters, close to size 40, a MIT has been indicated by the spectral analysis. We also presented the results of the jellium-based simulations for Rb and K clusters which described the responses in the valence spectra and revealed that an approach which takes account the continuum wave functions of the photoelectrons is required for the satisfactory description. Furthermore, the jellium simulations and the experimental observations for Rb clusters, confirmed the previously predicted oscillations of the jellium orbitals' cross sections as a function of photon energy. In addition to the scientific results of metal clusters, we presented the main principles of the EXMEC set-up and discussed about the technical implementation.

The research of metal clusters is expected to continue for other metallic elements in the future and concentrate on their metallic and chemical (i.e. catalytic) properties. Since the neutral metal clusters cannot be size selected in the present experimental set-up, in this work, we studied clusters with a size distribution and the cluster sizes had to be estimated using the CSA-model. However, the photoelectrons can be connected to the size of the host cluster by the so-called photoelectron-photoion coincidence (PEPICO) technique, which have been used lately in the study of small metal clusters [112–114]. This approach makes it possible to record photoelectron spectra from the known cluster sizes and avoid the effects related to the cluster size distribution. The EXMEC set-up used in this work was not compatible with the PEPICO experiments and therefore in the future a new version of the EXMEC set-up will be developed which will enable such experiments. The new set-up is also planned to be capable to form metal clusters made of two

different metallic elements (i.e. bi-metal clusters) and provide a possibility to deposit the formed clusters on surfaces.

Bibliography

[1] B. von Issendorff and O. Cheshnovsky, Annu. Rev. Phys. Chem. **56**, 549 (2005).

[2] K. Siegbahn, C. Nordling, A. Fahlman, R. Nordberg, K. Hamrin, J. Hedman, G. Johansson, T. Bergmark, S.-E. Karlsson, I. Lindgren, and B. Lindberg in *ESCA - Atomic, Molecular and Solid State Structure Studied by Means of Electron Spectroscopy* (Nova Acta Regiae Soc. Sci. Upsalienses, Ser. IV, Vol. 20, 1967).

[3] K. Siegbahn, C. Nordling, G. Johansson, J. Hedman, P. F. Hedénn, K. Hamrin, U. Gelius, T. Bergmark, L. O. Werme, R. Manne, and Y. Baer in *ESCA Applied to Free Molecules* (North-Holland Publ. Co., Amsterdam-London, 1969).

[4] K. D. Sattler in *Handbook of Nanophysics. Clusters and Fullerenes* (CRC Press, Boca Raton, FL, USA, 2011).

[5] E. W. Becker, K. Bier, and W. Henkes, Z. Phys. **146**, 333 (1956).

[6] O. Björneholm, F. Federmann, F. Fössing, and T. Möiler, Phys. Rev. Lett. **74**, 3017 (1995).

[7] G. Wrigge, M. Astruc Hoffmann, and B.V. Issendorff, Phys. Rev. A **65**, 063201 (2002).

[8] E. Schrödinger, Phys. Rev. **26**, 6 (1926).

[9] V. Schmidt in *Electron Spectrometry of Atoms using Synchrotron Radiation* (Cambridge University Press, 1997).

[10] P. A. M. Dirac, Proc. R. Soc. Lond. A **117**, 610 (1928).

[11] P. Atkins and R. Friedman in *Molecular Quantum Mechanics* (Oxford University Press, Oxford, 2005).

[12] C. Kittel in *Introduction to Solid State Physics* (Wiley, New York, 1996).

[13] P.-G. Reinhard and E. Suraud in *Introduction to Cluster Dynamics* (Wiley-vch, Weinhem, 2004).

[14] V. T. Deshpande and D. B. Sirdeshmukh, Acta Cryst. **14**, 355 (1961).

[15] T. P. Martins, T. Bergmann, H. Göhlich, and T. Lange, J. Phys. Chem **95**, 6421 (1991).

[16] B. Wang, J. Zhao, X. Chen, D. Shi, and G. Wang. Phys. Rev. A **71**, 033201 (2005).

[17] F. A. Fernandez-Lima, A. V. Henkes, E. F. da Silveira, and M. A. C. Nascimento, J. Phys. Chem. C **116** 4965 (2012).

[18] D. Reinhard, B. D. Hall, and D. Ugarte, Phys. Rev. B **55**, 7868 (1997).

[19] J. Farges, M. F. de Feraudy, B. Raoult, and G. Torchet, J. Chem. Phys. **78**, 5067 (1983).

[20] A. Jian, T. A. Tyson, and L. Axe, J. Phys.: Condens. Matter 17, 6111 (2005).

[21] S. J. Oh, S. H. Huh, H. K. Kim, J. W. Park, and G. H. Lee, J. Chem. Phys. **111**, 7402 (1999).

[22] S. H. Huh, H. K. Kim, J. W. Park, and G. H. Lee, Phys. Rev. B **62**, 2937 (2000).

[23] T. P. Martins, U. Näher, H. Schaber, and U. Zimmermann, J. Chem. Phys. **100**, 2322 (1994).

[24] M. Koskinen and M. Manninen, Phys. Rev. B **54**, 14796 (1996).

[25] D. Bonatsos, N. Karoussos, D. Lenis, P. P. Raychev, R. P. Roussev, and P. A. Terziev, Phys. Rev. A **62**, 013203 (2000).

[26] W. A. de Heer, Rev. Mod. Phys. **65**, 611 (1993).

[27] W. D. Knight, K. Clemenger, W. A de Heer, W. A. Saunders, M. Y. Chou, and M. L. Cohen, Phys. Rev. Lett. **52**, 2141 (1984).

[28] P. Jena and A. W. Castleman in *Nanoclusters: A Bridge Across Disciplines* (Elsevier, 2011).

[29] T. Diederich, T. Döppner, J. Braune, J. Tiggesbäumker, and K. H. Meiwes-Broer, Phys. Rev. Lett. **86**, 4807 (2001).

[30] L.-F. Cui, L.-M. Wang, and L.-S. Wang, J. Chem. Phys. **126**, 064505 (2007).

[31] O. Björneholm, G. Öhrwall, and M. Tchaplyguine, Nucl. Instr. Meth. Phys. Res. A **601**, 161 (2009).

[32] H. Hertz, Ann. Physik **267**, 983 (1887).

[33] A. Einstein, Ann. Physik **17**, 132 (1905).

[34] G. K. Wertheim, S. B. DiCenzo, and D. N. E. Buchanan, Phys. Rev. B **33**, 5384 (1986).

[35] V. D. Borman, M. A. Pushkin, V. N. Tronin, and V. I. Troyan, JETP **110**, 1005 (2010).

[36] B. Richter, H. Kuhlenbeck, H.-J. Freund, and P. S. Bagus, Phys. Rev. Lett. **93**, 026805 (2004).

[37] S. Peters, S. Peredkov, M. Neeb, W. Eberhardt, and M. Al-Hada, Surf. Sci., In Press (2012).

[38] M. Seidl, J. P. Perdew, M. Brajczewska, and C. Fiolhais, J. Chem. Phys. **108**, 8182 (1998).

[39] S. Aksela, M. Patanen, S. Urpelainen, and H. Aksela, New J. Phys. **12**, 063003 (2010).

[40] M. Aldén, H. L. Skriver, I. A. Abrikosov, and B. Johansson, Phys. Rev. B **51**, 1981 (1995).

[41] B. Johansson and N. Mårtensson, Phys. Rev. B **21**, 4427 (1980).

[42] P. H. Citrin and G. K. Wertheim, Phys. Rev. B **27**, 3176 (1983).

[43] E. Lundgren, R. Nyholm, M. Qvarford, J. N. Andersen, D. Heskett, and S. V. Christensen, Phys. Rev. B **56**, 12560 (1997).

[44] M. Tchaplyguine, R. R. Marinho, M. Gisselbrecht, J. Schulz, N. Mårtensson, S. L. Sorensen, A. Naves de Brito, R. Feifel, G. Öhrwall, M. Lundwall, S. Svensson, and O. Björneholm, J. Chem. Phys. **120**, 345 (2004).

[45] S. Peredkov, G. Öhrwall, J. Schulz, M. Lundwall, T. Rander, A. Lindblad, H. Bergensen, A. Rosso, W. Pokapanich, N. Mårtensson, S. Svensson, S. L. Sorensen, O. Björneholm, and M. Tchaplyguine, Phys. Rev. B **75**, 235407 (2007).

[46] M. Muntwiler and X.-Y. Zhu, New J. Phys. **10**, 113018 (2008).

[47] N. W. Ashcroft and N. D. Mermin in *Solid State Physics*, (Harcourt College Publishers, Orlando, 1976).

[48] G. D. Mahan in *Many Particle Physics*, 3rd edition (Kluwer Academic / Plenum Publishers, New York, 2000).

[49] W. Heisenberg, Z. Physik **43**, 172 (1927).

[50] G. D. Mahan, Phys. Rev. **163**, 612 (1967).

[51] P. H. Citrin, G. K. Wertheim, and Y. Baer, Phys. Rev. B **16**, 4256 (1977).

[52] S. Doniach, and M. Sunjic, J. Phys. C Solid State Phys. **3**, 285 (1970).

[53] T. T. P. Cheung, Surf. Sci. **127**, 129 (1983).

[54] V. D. Borman, V. V. Lebid'ko, M. A. Puskin, I. Smurov, V. N. Tronin, V. I. Troyan, JETP Lett. **80**, 557 (2004).

[55] P. Baltzer, L. Karlsson, M. Lundqvist, and B. Wannberg, Rev. Sci. Instrum. **64**, 2179 (1993).

[56] J. Végh, J. Electron Spectrosc. Relat. Phenom., **151**, 159 (2006).

[57] Spectrum Analysis by Curve Fitting (SPANCF) macro packages by Prof. Edwin Kukk (edwin.kukk@utu.fi), University of Turku.

[58] S. Barth, M. Oncak, V. Ulrich, M. Mucke, T. Lischke, P. Slavicek, and U. Hergenhahn, J. Phys. Chem. A **113**, 13520 (2009).

[59] E. Knoezinger and P. Beichert, J. Phys. Chem. **99**, 4906 (1995).

[60] J. M. Soler, N. Garcia, O. Echt, K. Sattler, and E. Recknagel, Phys. Rev. Lett. **49**, 49 (1992).

[61] H. Pauly in *Atom, Molecule, and Cluster Beams I* (Springer-Verlag, Berlin, 2000)

[62] H. Haberland in *Clusters of Atoms and Molecules: Theory, Experiment, and Clusters of Atoms* (Springer-Verlag, 1994)

[63] H. Murphy and D. Miller, J. Phys. Chem. **88**, 4474 (1984).

[64] L. S. Bartell, J. Phys. Chem. **94**, 5102 (1990).

[65] J. Tiggesbäumker and F. Stienkemeier, PCCP **9**, 4725 (2007).

[66] U. Buck and R. Krohne, J. Chem. Phys. **105**, 5408 (1996).

[67] O. Hagena and W. Obert, J. Chem. Phys. **56**, 1793 (1972).

[68] O. Hagena, Surf. Sci. **106**, 101 (1981).

[69] O. Hagena, Z. Phys. D **4**, 291 (1987).

[70] O. Hagena, Rev. Sci. Instrum. **63**, 2374 (1992).

[71] R. Karnbach, M. Joppien, J. Stapelfeldt, J. Wörmer, and T. Möller, Rev. Sci. Instrum. **64**, 2838 (1993).

[72] R. A. Smith, T. Ditmire, and J. W. G. Tisch, Rev. Sci. Instrum. **69**, 3798 (1998).

[73] F. Dorchies, F. Blasco, T. Caillaud, J. Stevefelt, C. Stenz, A. S. Boldarev, and V. A. Gasilov, Phys. Rev. A **68**, 023201 (2003).

[74] T. E. Gough, M. Mengel, P. A. Rowntree, and G. Scoles, J. Chem. Phys. **83**, 4958 (1985).

[75] A. Scheidemann, J. P. Toennies, and J. A. Northby, Phys. Rev. Lett. **64**, 1899 (1990).

[76] M. Rutzen, S. Kakar, C. Rienecker, R. von Pietrowski, and T. Möller, Z. Phys. D **38**, 89 (1996).

[77] A. Kolmakov, J. O. Löfken, C. Nowak, F. Picucci, M. Riedler, C. Rienecker, A. Wark, M. Wolff, and T. Möller, Chem. Phys. Lett. 319, 465 (2000).

[78] F. Stienkemeier, J. Higgins, W. E. Ernst, and G. Scoles, Phys. Rev. Lett. **74**, 3592 (1995).

[79] Y. Ren and V. V. Kresin, Phys. Rev. A **76**, 043204 (2007).

[80] S. Vongehr, A. A. Scheidemann, C. Wittig, and V. V. Kresin, Chem. Phys. Lett. 353, 89 (2002).

[81] C. Stark and V. V. Kresin, Phys. Rev. B **81**, 085401 (2010).

[82] L. A. der Lan, P. Bartl, C. Leidlmair, H. Schöbel, R. Jochum, S. Denifl, T. D. Märk, A. M. Ellis, and P. Scheier, J. Chem. Phys. **135**, 044309 (2011).

[83] L. A. der Lan, P. Bartl, C. Leidlmair, H. Schöbel, S. Denifl, T. D. Märk, A. M. Ellis, and P. Scheier, Phys. Rev. B **85**, 115414 (2012).

[84] J. Nagl, A. W. Hauser, G. Auböck, C. Callegari, and W. E. Ernst, J. Phys. Chem. A **111**, 12386 (2007).

[85] A. Bartelt, J. D. Close, F. Federmann, N. Quaas, and J. P. Toennies, Phys. Rev. Lett. **77**, 3525 (1996).

[86] D. Ievlev, I. Rabin, W. Schulze, and G. Ertl, Eur. Phys. J. D **16**, 157 (2001).

[87] W. Christen, P. Radcliffe, A. Przystawik, Th. Diederich, and J. Tiggesbäumber, J. Phys. Chem. A **115**, 8779 (2011).

[88] V. L. Mazalova, A. V. Soldatov, S. Adam, A. Yakovlev, T. Möller, R. L. Johnston, J. Phys. Chem. C **113**, 9086 (2009).

[89] J. Farges, M. F. de Feraudy, B. Raoult, and G. Torchet, J. Chem. Phys. **84**, 3491 (1986).

[90] M. Lewerenz, B. Schilling, and J. P. Toennies, J. Chem. Phys. **102**, 8191 (1995).

[91] O. Bünermann and F. Stienkemeir, E. Phys. J. D **61**, 645 (2011).

[92] J. P. Toennies and A. F. Vilesov, Angew. Chem. **43**, 2622 (2004).

[93] F. R. Elder, A. M. Gurewitcsh, R. V. Langmuir, and H. C. Pollock, Phys. Rev. **71**, 829 (1947).

[94] D. Attwood in *Soft X-rays and Extreme Ultraviolet Radiation* (Cambridge University Press, New York, 1999).

[95] M. Bässler, J.-O. Forsell, O. Björneholm, R. Feifel, M. Jurvansuu, S. Aksela, S. Sundin, S.L. Sorensen, R. Nyholm, A. Ausmees, and S. Svensson, J. Electron Spectrosc. Related Phenom. **101**, 953 (1999).

[96] M. Bässler, A. Ausmees, M. Jurvansuu, R. Feifel, J.-O. Forsell, P. de Tarso Fonseca, A. Kivimäki, S. Sundin, S.L. Sorensen, R. Nyholm, O. Björneholm, S. Aksela, and S. Svensson, Nucl. Instrum. Methods **469**, 382 (2001).

[97] R. Sankari, R. Nyholm, and S. Aksela, Rad. Phys. Chem. **75**, 2000 (2006).

[98] M. Huttula, K. Jänkälä, A. Mäkinen, H. Aksela, and S. Aksela, New J. Phys. **10**, 013009 (2008).

[99] Q.-K. Xue, Nat. Nanotechnol. **6**, 197 (2012).

[100] D. Pesin and A. H. MacDonald, Nature Mater. **11**, 409 (2012).

[101] Z. Liu, C.-X. Liu, Y.-S. Wu, W-H. Duan, F. Liu, and J. Wu, Phys. Rev. Lett. **107**, 136805 (2011).

[102] J. W. Wells, J. H. Dil, F. Meier, J. Lobo-Checa, V. N. Petrov, J. Oster-walder, M. M. Ugeda, I. Fernandez-Torrente, J. I. Pascual, E. D. L. Rienks, M. F. Jensen, and Ph. Hofmann, Phys. Rev. Lett. **102**, 096802 (2009).

[103] J. E. Moore, Nature **464**, 194 (2010).

[104] Ph. Hofmann, Prog. Surf. Sci. **81**, 191–245 (2006).

[105] M. Z. Hasan and C. L. Kane, Rev. Mod. Phys. **82**, 3045 (2010).

[106] C. Vossloh, M. Holdenried, and H. Micklitz, Phys. Rev. B **58**, 12422 (1998).

[107] T. E. Huber, A. Nikolaeva, D. Gitsu, L. Konopko, C. A. Foss, and M. J. Graf, Appl. Phys. Lett **84**, 1326 (2004).

[108] C. A. Hoffman, J. R. Meyer, F. J. Bartoli, A. Di Venere, X. J. Yi, C. L. Hou, H. C. Wang, J. B. Ketterson, and G. K. Wong, Phys. Rev. B **48**, 11431 (1993).

[109] S. Fujimassa, M. Imamura, and H. Yasuda, J. Electron Spectrosc. Relat. Phenom. **184**, 309 (2011).

[110] F. Patthey and W.-D. Schneider, Phys. Rev. B **49**, 11293 (1994).

[111] O. Frank and J. M. Rost, Z. Phys. D **38**, 59 (1996).

[112] S. Urpelainen, A. Caló, L. Partanen, M. Huttula, S. Aksela, H. Aksela, S. Granroth, and E. Kukk, Phys. Rev. A **79**, 023201 (2009).

[113] S. Urpelainen, A. Caló, L. Partanen, M. Huttula, J. Niskanen, E. Kukk, S. Askela, and H. Aksela, Phys. Rev. A **80**, 043201 (2009).

[114] K. Kooser, D. T. Ha, E. Itälä, J. Laksman, S. Urpelainen, and E. Kukk, J. Chem. Phys. **137**, 044304 (2012).